

1
2
3
4
5
6
7
8
9
10
11
12
13
14
15
16
17
18
19
20
21
22
23
24
25
26
27
28
29
30
31

Finite Element Modeling of Lateral Pipeline–Soil Interactions in Dense Sand

Kshama Roy¹, Bipul Hawlader^{2*}, Shawn Kenny³ and Ian Moore⁴

¹PhD Candidate, Department of Civil Engineering, Faculty of Engineering and Applied Science, Memorial University of Newfoundland, St. John’s, Newfoundland and Labrador A1B 3X5, Canada

²**Corresponding Author:** Associate Professor, Department of Civil Engineering, Faculty of Engineering and Applied Science, Memorial University of Newfoundland, St. John’s, Newfoundland and Labrador A1B 3X5, Canada
Tel: +1 (709) 864-8945 Fax: +1 (709) 864-4042 E-mail: bipul@mun.ca

³Associate Professor, Department of Civil and Environmental Engineering, Faculty of Engineering and Design, Carleton University, 1125 Colonel By Drive, Ottawa, ON, K1S 5B6, Canada

⁴Professor and Canada Research Chair in Infrastructure Engineering, GeoEngineering Centre at Queen’s – RMC, Queen’s University, Kingston, ON, K7L 4V1, Canada

Number of Figures: 19

Number of table: 1

KEYWORDS: pipeline, Mohr-Coulomb model, finite element analyses, dense sand, lateral movement

32 **Abstract:**

33 Finite element (FE) analyses of pipeline–soil interaction for pipelines buried in dense sand
34 subjected to lateral ground displacements are presented in this paper. Analysis is performed
35 using the Arbitrary Lagrangian-Eulerian (ALE) method available in Abaqus/Explicit FE
36 software. The pipeline–soil interaction analysis is performed in the plane strain condition using
37 the Mohr-Coulomb (MC) and a modified Mohr-Coulomb (MMC) models. The MMC model
38 considers a number of important features of stress–strain and volume change behaviour of dense
39 sand including the nonlinear pre- and post-peak behaviour with a smooth transition and the
40 variation of the angle of internal friction and dilation angle with plastic shear strain, loading
41 conditions (triaxial or plane strain), density and mean effective stress. Comparing FE and
42 experimental results, it is shown that the MMC model can better simulate the force–displacement
43 response for a wide range of lateral displacements of the pipe for different burial depths,
44 although the peak force on the pipe could be matched using the MC model. Examining the
45 progressive development of zones of large inelastic shear deformation (shear bands), it is shown
46 that the mobilized angle of internal friction and dilation angle vary along the length of the shear
47 band, however constant values are used in the MC model. A comprehensive parametric study is
48 also performed to investigate the effects of pipeline diameter, burial depth and soil properties.
49 Many important aspects in the force–displacement curves and failure mechanisms are explained
50 using the present FE analyses.

51

52 **1. Introduction**

53 Pipelines are extensively used for transporting water and hydrocarbons. Any relative
54 displacements (e.g. during slope movement) between pipeline and soil exert forces on pipelines.

55 The pipeline–soil interaction analyses are generally performed defining the force–displacement
56 curves in the lateral, vertical and axial directions based on available guidelines (American
57 Lifelines Alliance 2005; Honegger and Nymann 2004). Pipelines can be buried in a wide variety
58 of soils and subjected to loading from different directions. Pipelines buried in dense sand
59 subjected to large lateral displacement are the focus of the present study, since nonuniform
60 lateral displacement leads to longitudinal bending and other structural demands that can exceed
61 the structural capacity. Experimental studies have been conducted in the past to understand
62 lateral pipeline–soil interaction in sand (e.g. Audibert and Nyman 1977; Trautmann 1983;
63 Scarpelli et al. 1999; Turner 2004; Wijewickreme et al. 2009; Daiyan 2013; Almahakeri et al.
64 2013, 2014). From the test results, the force–displacement curves could be obtained and the
65 failure mechanisms could be interpreted. The displacements of soil particles with lateral
66 movement of the pipe could be visualized using the advanced particle image velocimetry (PIV)
67 techniques (Burnett 2015). Guo and Stolle (2005) compiled the data from experimental studies
68 and showed a wide variation in the non-dimensional peak force, which depends upon sand
69 properties, diameter of the pipe, burial depth, and test procedure. In addition to the peak force,
70 the shape of the force–displacement curve is also influenced by these factors. In structural
71 modeling, the force–displacement curves as elastoplastic soil springs are given as input, which is
72 valid up to mobilization of the peak force. However, a section of pipeline might experience large
73 displacements where post-peak soil resistance governs the response. Recognizing this, design
74 guidelines (e.g. DNV 2007) suggested that the post-peak response of dense sand should be
75 considered in uplift resistance calculation as the sand moves to a looser state at displacements
76 beyond the peak displacement. As shown later, the mobilization of angles of internal friction (ϕ')
77 and dilation (ψ) both in pre- and post-peak levels is equally important for calculation of lateral

78 resistance. Moreover, a better representation of force–displacement curves up to sufficiently
79 large displacements will improve structural modeling of pipeline.

80 Continuum finite element (FE) analyses have been performed in the past to simulate lateral
81 pipeline–soil interaction in sand (e.g. Yimsiri et al. 2004; Guo and Stolle 2005; Xie 2008; Daiyan
82 et al. 2011; Jung et al. 2013). The soil constitutive model used in the analysis influences FE
83 simulation results (Yimsiri et al. 2004). Figure 1 shows the typical stress–strain and volume
84 change behaviour of dense sand in consolidated isotropically drained (CID) triaxial compression
85 tests. The stress ratio (q/p'), (where p' is the mean effective stress and q is deviatoric stress)
86 increases gradually (hardening) up to the peak and then decreases (softening) to the critical state
87 at large axial strains (Fig. 1a). The axial strain at the peak stress ratio (ε_a^p) decreases with
88 confining pressure (σ_c). Experimental evidence also shows that ε_a^p decreases with relative
89 density (Lee 1965; Kolymbas and Wu 1990; Lancelot et al. 2006). Figure 1(b) shows higher
90 dilation in tests with low σ_c . Moreover, the volumetric expansion starts at lower axial strains for
91 low confining pressures. These characteristics observed not only in the triaxial stress condition;
92 the results from direct shear tests also show similar behaviour for different vertical normal
93 stresses (Lings and Dietz 2004).

94 Another important experimental observation is that the behaviour of dense sand in triaxial
95 and simple shear conditions is different. For example, Ahmed (1973) conducted tests on crushed
96 silica sand in drained triaxial (TX) and plane strain (PS) loading conditions. The peak friction
97 angles (ϕ'_p) from his test results are shown in Fig. 2. Three key features of these test results need
98 to be mentioned: (i) ϕ'_p for the plane strain condition (ϕ'^{PS}_p) is higher than ϕ'_p for the triaxial
99 condition (ϕ'^{TX}_p), and the value of $\phi'^{PS}_p - \phi'^{TX}_p$ is higher at low stress levels, (ii) both ϕ'^{PS}_p and

100 ϕ_p^{TX} increase with D_r , and (iii) ϕ_p' for both TX and PS configurations decrease with of confining
101 pressure.

102 In summary, pre-peak hardening, post-peak softening, density and confining pressure
103 dependent ε_a^p , angle of internal friction and dilation angle are the common features of the stress–
104 strain behaviour of dense sand. The mode of shearing (TX or PS) also significantly influences
105 the behaviour. All these features of the stress–strain behaviour of dense sand have not been
106 considered in the available FE modeling of pipeline–soil interaction. For example, Yimsiri et al.
107 (2004) used the Mohr-Coulomb model with constant angles of internal friction and dilation
108 (MC). They also conducted FE analyses using the Nor-Sand soil constitutive models. Guo and
109 Stolle (2005) and Daiyan et al. (2011) considered the effects of p' and plastic shear strain on ϕ'
110 and ψ but did not incorporate the effects of density on the plastic strain required to mobilize the
111 peak value. Robert (2010) and Jung et al. (2013) incorporated the post-peak softening using a
112 linear variation of angles of internal friction and dilation with plastic strain, but did not consider
113 the pre-peak hardening. However, Jung et al. (2013) conducted the simulation using plane strain
114 strength parameters.

115 From a numerical point of view, the softening of soil causes strain localization into shear
116 bands resulting in significant mesh distortion in typical FE formulations expressed in the
117 Lagrangian framework (Qiu et al. 2009; Pike et al. 2013). It is preferable to avoid such mesh
118 distortion issues in FE simulation. The distinct element method has also been used in the past to
119 accommodate large soil movement around the pipe and to continue the analysis up to large pipe
120 displacements (Yimsiri and Soga 2006).

121 The main objective of the present study is to simulate lateral pipeline–soil interaction using
122 Abaqus/Explicit (taking the advantages of better modeling capability of strength degradation in
123 shear bands over Abaqus/Standard) implementing a modified Mohr-Coulomb (MMC) model that
124 can capture the features of dense sand behaviour discussed above. The paper has been organized
125 in the following way. First, the development of the MMC model is presented. The key model
126 parameters and their relations to experimental results are discussed. Second, the FE simulations
127 of triaxial test results are performed to show the performance of the proposed MMC model.
128 Third, the FE simulations are performed for lateral pipeline–soil interaction and compared with
129 test results. Finally, a comprehensive parametric study is performed.

130

131 **2. Modeling of Soil Behaviour**

132 The elastic perfectly plastic Mohr-Coulomb (MC) model, in its original form and also after
133 some modifications, has been used by a number of researchers in the past for pipeline–soil
134 interaction analysis (e.g. Moore and Booker 1987; Taleb and Moore 1999; Ellis and Springman
135 2001; Yimsiri et al. 2004; Guo and Stolle 2005; Daiyan et al. 2011; Almahakeri et al. 2012;
136 Kouretzis et al. 2013). In MC model, the soil behaviour is elastic until the stress state reaches the
137 yield surface which is defined by the Mohr-Coulomb failure criterion. This model is available in
138 commercial software packages including Abaqus FE program. The modification of MC model
139 has been performed by implementing some additional features of dense sand behaviour (Guo and
140 Stolle 2005; Daiyan et al. 2011; Jung et al. 2013). The present FE analyses are performed using a
141 MMC model incorporating all of the features of dense sand behaviour discussed in the following
142 sections.

143 a) Angle of internal friction in triaxial compression (TX) and plane strain (PS) conditions

144 The strength of sand is characterized by mobilized angle of internal friction (ϕ') and dilation
145 angle (ψ). First, two limiting values of ϕ' are examined: (i) at the peak (ϕ'_p) and (ii) the critical
146 state (ϕ'_c).

147 Experimental results show that ϕ'_p depends on density of sand and also on the direction of
148 shearing (e.g. Bolton 1986; Houlsby 1991; Schanz and Vermeer 1996). Kulhawy and Mayne
149 (1990) compiled a large volume of test data and showed that, for dense sand, ϕ'_p^{PS} is
150 approximately 10 to 20% higher than ϕ'_p^{TX} . Furthermore, experimental evidence also shows that
151 ϕ'_p decreases with confining pressure (σ_c) (Fig. 1) or p' at failure (Bolton 1986).

152 Assuming unique ϕ'_c for both TX and PS conditions, Bolton (1986) proposed the following
153 relationships from test results for 17 sands.

$$154 \quad [1] \quad \phi'_p - \phi'_c = A_\psi I_R$$

155 where $A_\psi=3$ for TX and 5 for PS conditions. I_R is the relative density index defined as
156 $I_R = I_D(Q - \ln p') - R$ in which I_D =relative density ($=D_r(\%)/100$), $Q=10$ and $R=1$. Bolton (1986)
157 also recognized that stress and strain non-uniformity could be strong at very low p' . Moreover, at
158 that time, accurate measurement of small stresses and strains was difficult. As such Bolton
159 (1986) set the maximum limit of $I_R=4$. White et al. (2008) also used $I_R=0-4$ as a permissible
160 range for modeling pipelines buried in sand. Therefore, according to Eq. (1), the maximum value
161 of $\phi'_p - \phi'_c$ of 12° and 20° for the TX and PS conditions, respectively, are used in the present
162 study.

163 Equation (1) has been verified with additional test data and used by many researchers. For
164 example, Houlsby (1991) developed a relationship similar to Eq. (1) based on the critical state
165 theory. Similarly, based on Eq. (1), Schanz and Vermeer (1996) showed that

166 $\phi_p'^{PS} = (5\phi_p'^{TX} - 2\phi_c')$ is valid for a wide range of test results on Hostun dense sand. In other
167 words, for dense sand at low stress levels, $\phi_p'^{PS}$ is higher than $\phi_p'^{TX}$. Attempts have also been
168 made in the past to develop relationships between $\phi_p'^{PS}$ and ϕ' obtained from direct shear tests
169 ($\phi_p'^{DS}$) (Taylor 1948; Davis 1968; Rowe 1969). Lings and Dietz (2004) provided a detailed
170 discussion of these relationships. From comparisons with test results, they showed that $\phi_p'^{PS} \approx$
171 $\phi_p'^{DS} + 5^\circ$, where $\phi_p'^{DS}$ is the peak friction angle from a direct shear test. In summary, although
172 triaxial and direct shear tests are widely used to determine ϕ' , it should be properly adjusted if the
173 analysis is performed for plane strain conditions where $\phi_p'^{PS}$ is required.

174 The value of A_ψ in Eq. (1) might vary with type of sand and fine contents. For example,
175 Chakraborty and Salgado (2010) found $A_\psi=3.8$ for Toyoura sand for both TX and PS conditions,
176 while Xiao et al. (2014) showed $A_\psi=3.0-5.53$ for Ottawa sand with 0–20% fine contents for the
177 triaxial condition. Xiao et al. (2014) also proposed an empirical relationship for A_ψ as a function
178 of fine content. Moreover, Q is also varied using an empirical function of σ_c (Chakraborty and
179 Salgado 2010; Xiao et al. 2014), instead of a constant value as proposed by Bolton (1986).
180 Although these empirical functions of A_ψ and Q might fit the test results better, a constant value
181 of Q ($=10$) and $A_\psi=5$ with the limiting maximum value of $\phi_p' - \phi_c'$ of 12° and 20° for TX and
182 PS configurations, respectively, are used in the present study.

183 Experimental evidence shows that $\phi_c'^{PS}$ is a few degrees higher than $\phi_c'^{TX}$. Bishop (1961) and
184 Cornforth (1964) conducted laboratory tests over the full range of relative densities at a wide
185 range of σ_c and showed that $\phi_c'^{PS}$ is approximately 4° greater than $\phi_c'^{TX}$. A similar trend was

186 found from laboratory tests on Toyoura sand, and it has been shown that $\phi'_c{}^{PS} \approx 34.5^\circ - 38^\circ$
187 while $\phi'_c{}^{TX} \approx 33^\circ$ (Tatsuoka et al. 1986; Pradhan et al. 1988; Yoshimine 2005).

188 In this study, $\phi'_c{}^{TX} = 31^\circ$ $\phi'_c{}^{PS} = 35^\circ$ are used. The authors also aware of the fact that ϕ'_c might
189 slightly increase with decrease in p' (Lings and Dietz 2004); however, such variation is not
190 considered in this study.

191 Bolton (1986) also showed that the maximum dilation angle (ψ_p) is related to the peak and
192 critical state friction angle as:

193 [2] $\phi'_p - \phi'_c = k_\psi \psi_p$

194 where $k_\psi = 0.8$ for PS and 0.5 for TX configurations (Bolton 1906). Note that k_ψ might be also
195 dependent on type of sand, fines content and/or gravel fraction (Simoni and Houlsby 2006;
196 Chakraborty and Salgado 2010; Xiao et al. 2014).

197
198 b) Stress–strain behaviour of dense sand

199 Generally in the widely used MC model it is assumed that: (i) plastic strains develop only
200 when the stress state is on the failure (yield) surface, (ii) any change in stresses inside the yield
201 surface results in only elastic strain, and (iii) soil deforms at a constant dilation angle once the
202 stress state reaches the yield surface. However, experimental evidence shows that plastic strains
203 usually develop well before failure. In order to capture this behaviour, constitutive models of
204 different forms have been proposed in the past (Prevost 1985; Gajo and Wood 1999; Dafalias
205 and Manzari 2004). Similar to these works, it is assumed that the plastic deformation occurs only
206 for changes of q/p' . The development of plastic strain for loading under constant stress ratio is

207 neglected because the soil considered in this study is not loose and crushing of sand grains is not
208 expected because of stress increase due to displacement of the pipeline.

209 Following the conceptual frameworks developed in previous studies (e.g. Jardine 1992;
210 Mitchell and Soga 2005), the stress–strain behaviour of dense sand is divided into three zones as
211 shown in Fig. 3.

212 Zone-I: In this zone, elastic (linear and/or nonlinear) deformation occurs. In the pure linear
213 elastic zone the soil particles do not slide relative to each other. However, in nonlinear elastic
214 deformation small slide or rolling between particles might occur but the deformation is
215 recoverable during unloading. The deformation behaviour in this zone can be defined by elastic
216 properties namely Young’s modulus (E), and Poisson’s ratio (ν).

217 Zone-II: If the shearing is continued, the soil element will move to zone-II (Fig. 3) which
218 can be considered as the “pre-peak plastic zone” (Mitchell and Soga 2005). The mobilized ϕ'
219 (Fig. 3) is used to define the yield surface using the Mohr-Coulomb model. When the stress state
220 approaches the initial yield surface (i.e. yield surface with ϕ'_{in} at point A in Fig. 3), plastic strains
221 occur upon further loading. The initial yield surface of dense sand is inside the failure envelope
222 defined by the peak friction angle. The pre-peak plastic deformation of geomaterials has been
223 recognized by many researchers from experimental data, and multiple yield surfaces are used to
224 simulate this; for example, the multi-yield surface model (Mroz 1967), the nested surface
225 plasticity model (e.g. Prévost 1985), the bounding surface plasticity model (Dafalias and
226 Herrman 1982), and the subloading surface model (Hashiguchi and Ueno 1977). These complex
227 models can simulate many important features including the stress–strain behaviour during cyclic
228 loading. However, in the present MMC model the mobilized ϕ' and ψ are varied with
229 accumulated engineering plastic shear strain (γ^p) as shown in Fig. 3. A set of equations (Eq. 3–8)

230 are proposed to model this behaviour after some modifications of similar type of models
231 proposed in previous studies (Vermeer and de Borst 1984; Tatsuoka et al. 1993; Hsu and Liao
232 1998).

233 In the pre-peak zone-II, ϕ' and ψ increase from ϕ'_{in} and ψ_{in} to the peak values ϕ'_p and ψ_p at
234 strain γ_p^p . Based on Rowe (1969), Mitchell and Soga (2005) suggested that the mobilized ϕ' of
235 sand is the sum of the contributions of four components: interparticle friction, rearrangement of
236 particles (fabric), crushing, and dilation. As p' is not very high in the pipeline–soil interaction
237 analysis being undertaken here, the crushing effect is negligible. At the beginning of plastic
238 deformation $\psi_{in}=0$ is assumed. Therefore, interparticle friction and soil fabric are the main
239 contributors to ϕ'_{in} (point A in Fig. 4). Based on typical contributions of each component of ϕ'
240 (Mitchell and Soga, 2005), $\phi'_{in}=29^\circ$ is assumed in this study.

241 For given relative density and confining pressure, I_R can be calculated, which can be then
242 used to calculate ϕ'_p using Eq. (1). Now using Eq. (2), the value of ψ_p can be calculated.
243 However, as discussed in the introduction, the shear strain or displacement required to mobilize
244 ϕ'_p decreases with density and increases with confining pressure (Lee et al. 1965; Tatsuoka et al.
245 1986; Hsu and Liao 1998; Lings and Dietz 2004). The effects of density and stress level are
246 incorporated in γ_p^p as:

247 [3] $\gamma_p^p = \gamma_c^p (p' / p'_a)^m$

248 [4] $\gamma_c^p = C_1 - C_2 I_D$

249 where γ_c^p = strain softening parameter; p'_a = reference pressure which is considered as the
250 atmospheric pressure (=100 kPa); m , C_1 and C_2 are soil parameters, which could be obtained

251 from a set of triaxial or simple shear tests at different confining pressures and densities. Further
 252 explanation of these parameters are provided in the following sections.

253 The following sine functions are then used to model the variation of mobilized ϕ' and ψ in
 254 zone-II.

$$255 \quad [5] \quad \phi' = \phi'_{in} + \sin^{-1} \left[\left(\frac{2\sqrt{\gamma^p \gamma_p^p}}{\gamma^p + \gamma_p^p} \right) \sin(\phi'_p - \phi'_{in}) \right]$$

$$256 \quad [6] \quad \psi = \sin^{-1} \left[\left(\frac{2\sqrt{\gamma^p \gamma_p^p}}{\gamma^p + \gamma_p^p} \right) \sin(\psi_p) \right]$$

257 The lines AB and DE in Fig. 3 demonstrate the variation of ϕ' and ψ , respectively, in the pre-
 258 peak zone for $D_r=80\%$ and $p'=40$ kPa.

259

260 Zone-III:

261 If the shearing is continued, both ϕ' and ψ will decrease with γ^p in Zone-III (Fig. 3). This
 262 zone is referred as the “post-peak softening zone.” The following exponential functions are used
 263 to define the curves *BC* and *EF* to model the variation of ϕ' and ψ with plastic strain,
 264 respectively.

$$265 \quad [7] \quad \phi' = \phi'_c + (\phi'_p - \phi'_c) \exp \left[- \left(\frac{\gamma^p - \gamma_p^p}{\gamma_c^p} \right)^2 \right] \quad \text{curve } BC$$

$$266 \quad [8] \quad \psi = \psi_p \exp \left[- \left(\frac{\gamma^p - \gamma_p^p}{\gamma_c^p} \right)^2 \right] \quad \text{curve } EF$$

267 The strain softening parameter γ_c^p controls the shape of the post-peak curves. The lower the
 268 value of γ_c^p , the faster the decrease of ϕ' from ϕ'_p to ϕ'_c . After some algebraic calculation, it can

269 be shown from Eqs. (7) and (8) that the point of inflection of the post-peak softening curve
270 occurs at $\gamma_c^p / \sqrt{2}$ from γ_p^p as shown by the open circles in Fig. 3. The shapes of the curves
271 defined by Eqs. (6–8) are very similar to the observed behaviour of dense sand.

272 The novel aspects that the present MMC model adds to the existing models of similar type
273 for pipeline–soil interaction analysis (e.g. Guo and Stolle 2005; Robert 2010; Daiyan et al. 2011;
274 Jung et al. 2013a,b; Pike et al. 2013) are primarily twofold. Firstly, nonlinear pre- and post-yield
275 behaviour with a smooth transition is incorporated. Secondly, the mobilization of ϕ' and ψ with
276 plastic strain, including the peak values, depends on density and mean effective stress.

277 c) Elastic properties

278 Poisson's ratio (ν) and Young's modulus (E) of the soil are the two elastic parameters. The
279 Poisson's ratio of 0.2 is used, which has been considered as the best representative value for
280 dense sand (Jefferies and Been 2006). E is varied with p' using the following power function
281 (Hardin and Black 1966; Janbu 1963).

$$282 \quad [9] \quad E = K p_a \left(\frac{p'}{p_a} \right)^n$$

283 where K is a material constant, P_a is the atmospheric pressure (=100 kPa) and n is an exponent.
284 A number of authors used Eq. (9) in FE modeling of pipeline–soil interaction (Taleb and Moore
285 1999; Yimsiri et al. 2004; Guo and Stolle 2005; Daiyan et al. 2011; Jung et al. 2013). Further
286 discussion on the selection of elastic parameters can be found in those studies and is not repeated
287 here.

288

289 3. FE Modeling of Pipeline–Soil Interaction

290 Two-dimensional pipeline–soil interaction analyses are conducted using the Abaqus/Explicit
291 FE software. The main advantages of using Abaqus/Explicit over Abaqus/Standard is that the
292 pipe can be moved relatively large distances while still largely avoiding numerical issues
293 associated with mesh distortion as encountered when employing Abaqus/Standard, especially in
294 the zones of shear strain localization. Therefore, the large strains that concentrate in the shear
295 bands can be better simulated using Abaqus/Explicit.

296 A typical FE mesh for 300 mm outer pipe diameter (D) is shown in Fig. 4. For FE modeling
297 of soil, the 4-node bilinear plane strain quadrilateral element (CPE4R) is used. The pipe is
298 modeled as a rigid body. Abaqus/cae is used to generate the FE mesh. The structured mesh (Fig
299 4) is generated by zoning the soil domain. A denser mesh is used near the pipe. The bottom of
300 the FE domain is restrained from any movements, while all the vertical faces are restrained from
301 any lateral movement using roller supports (Fig. 4). No displacement boundary condition is
302 applied on the top face. The pipe is placed at the desired location (i.e. wished-in-place
303 configuration). The depth of the pipe is measured in terms of H/D ratio, where H is the depth
304 from the top of the soil to the centre of the pipe. The locations of the bottom and right boundaries
305 with respect to the location of the pipe are sufficiently large and therefore boundary effects on
306 calculated lateral resistance, displacement and soil failure mechanisms are not found. This has
307 been verified by a number of FE analyses setting these boundaries at larger distances than those
308 shown in Fig. 4. The pipe is pulled laterally, without any rotation, applying a displacement
309 boundary condition at the reference point (the center of the pipe). No additional boundary
310 condition is applied in the vertical direction, and the pipe is free to displace in the vertical

311 direction during lateral movement. The horizontal component of the reaction force at the
312 reference point of the rigid pipe gives the lateral resistance.

313 The interface between pipe and soil is simulated using the contact surface approach available
314 in Abaqus/Explicit. The Coulomb friction model is used for the frictional interface between the
315 outer surface of the pipe and sand. In this method, the friction coefficient (μ) is defined as
316 $\mu = \tan(\phi_\mu)$, where ϕ_μ is the friction angle of the pipe-soil interface. The value of ϕ_μ depends on
317 the interface characteristics and relative movement between the pipe and soil. The larger values
318 of ϕ_μ represent the characteristics of rough uncoated pipes with rusty or corroded surfaces, while
319 the lower values would correspond to pipes with smooth coating. The value of ϕ_μ lies between 50
320 and 100% of the peak friction angle (Yimsiri et al, 2004). A value of μ equal to 0.32 is used in
321 this study.

322 The numerical analysis is conducted in two steps. In the first step, geostatic stress is applied
323 under $K_0=1$ condition. The value of K_0 might be smaller than 1; however, a parametric study
324 shows that K_0 does not have significant effects on lateral resistance (Jung et al. 2013). In the
325 second step, the pipe is displaced in the lateral direction specifying a displacement boundary
326 condition at the reference point of the pipe.

327 Abaqus does not have any direct option for modeling stress-strain behaviour using the
328 proposed MMC model; therefore, in this study it is implemented by developing a user subroutine
329 VUSDFLD written in FORTRAN. The stress and strain components are called in the subroutine
330 in each time increment. From the stress components, p' is calculated. The strain components are
331 transferred to the principal strain components and stored as state variables. The plastic strain
332 increment ($\Delta\gamma^p$) in each time increment is calculated as $\Delta\gamma^p = (\Delta\varepsilon_1^p - \Delta\varepsilon_3^p)$, where $\Delta\varepsilon_1^p$ and $\Delta\varepsilon_3^p$
333 are the major and minor principal plastic strain components, respectively. The value of γ^p is

334 calculated as the sum of incremental $\Delta\gamma^p$ over the period of analysis. In the subroutine, γ^p and
335 p' are defined as two field variables FV1 and FV2, respectively. In the input file, using Eqs. (1-8),
336 the mobilized ϕ' and ψ are defined in tabular form as a function of γ^p and p' . During the analysis,
337 the program accesses the subroutine and updates the values of ϕ' and ψ with field variables.

338 Two sets of FE analyses in the plane strain condition are performed for lateral displacement
339 of the pipe. In the first set, analyses are performed for $D=102$ mm pipes and compared with
340 Trautmann (1983) model test results, which is denoted the “model test simulation.” In the second
341 set, a parametric study is performed varying pipe diameter, burial depth and soil properties. In
342 addition, triaxial test results are simulated for soil parameter estimation and also to examine the
343 performance of the proposed MMC model.

344

345 **4. FE simulation of triaxial test**

346 Trautmann (1983) conducted a series of model tests to understand the mechanisms involved
347 in lateral displacement of pipes buried in sand. The tests in dry dense sand are simulated in the
348 present study. Cornell filter sand was used in these tests. These test results have been used by
349 previous researchers to validate the performance of numerical modeling. For example, Yimsiri et
350 al. (2004) simulated these tests using the MC and Nor-Sand models. For the Mohr-Coulomb
351 model, they obtained the values of ϕ' and ψ from direct shear test results, assuming that the plane
352 strain nature of pipeline–soil interaction problem is more consistent with direct shear than
353 triaxial compression. However, ϕ'_p in PS could be approximately 5° higher than ϕ'_p in the direct
354 shear condition (Pradhan et al. 1998; Lings and Dietz 2004). Yimsiri et al. (2004) also estimated
355 the Nor-Sand model parameters by fitting FE simulation against the triaxial test results for
356 Cornell filter sand (Turner and Kulhawy 1987).

357 To show the performance of the proposed MMC model, consider the same triaxial test on
358 dense sand used by Yimsiri et al. (2004). Figure 5 shows the comparison between test results and
359 FE simulations using three models: MC, Nor-Sand, and MMC. A CAX4 element in Abaqus is
360 used in the FE modeling. The Young's modulus is calculated using Eq. (9) substituting p' for
361 confining pressure. As estimated by Yimsiri et al. (2004) for dense Cornell filter sand, constant
362 ϕ' (=44°) and ψ (=16°) are used in the MC model. The FE simulation with Nor-Sand model is
363 plotted from Yimsiri et al. (2004). The FE analysis with the present MMC model is performed
364 using the VUSDFLD subroutine, as discussed in previous section, with triaxial condition in Eqs.
365 (1) and (2). All other parameters used in the analysis are listed in Table 1.

366 Figure 5(a) shows that for the MC model q/p' increases with ε_a to the peak value and then
367 remains constant because a constant ϕ' is used in the analysis. Figure 5(b) shows that volumetric
368 compression occurs initially and then the soil dilates linearly, because a constant ψ is used. In
369 other words, the constant strength and dilatancy criteria take over the stress-strain behaviour
370 once it reaches the maximum stress ratio. As stated by Wood (2007), the MC model is sufficient
371 if the failure is the only concern; however, its ability to match the complete mechanical response
372 of a soil element is poor. Both strength and deformation behaviour of soil are equally important
373 in the pipeline-soil interaction analysis. Therefore, an advanced model that considers the
374 variation of strength of dense sand with shear deformation could give improved simulation
375 results.

376 Unlike the simulation with the MC model, the shape of q/p' - ε_a and ε_v - ε_a curves using the
377 Nor-Sand model is very similar to test results (Fig. 5). However, a complex VUMAT subroutine
378 needs to be developed for the Nor-Sand model while the MMC can be implemented through a
379 relatively simple user subroutine VUSDFLD as discussed above. As shown later, most of the

380 features involved in pipeline–soil interaction could be simulated using the proposed MMC
381 model. In addition, the pre-peak hardening behaviour is considered in the present MMC model.

382 The simulations with the MMC model are performed for two sets of A_ψ and k_ψ values in Eqs.
383 1 and 2, respectively. First, $A_\psi=3$ and $k_\psi=0.5$ (Bolton 1986) is used. Chakraborty and Salgado
384 (2010) showed that $A_\psi=3.8$ and $k_\psi=0.6$ match better the triaxial test results on Toyoura sand at
385 low stresses. Therefore, FE simulation is performed also with $A_\psi=3.8$ and $k_\psi=0.6$ to show their
386 effects. As shown in Fig. 5(a), the proposed MMC model can successfully simulate the stress–
387 strain behaviour. Calculated q/p' nonlinearly increases with ε_a , reaches the peak, and then
388 decreases in the post-peak region. Volumetric compression occurs initially and then the
389 specimen expands nonlinearly with ε_a (Fig. 5b). At large ε_a , $\Delta\varepsilon_v/\Delta\varepsilon_a=0$, which is different from
390 the simulation with the MC model that calculates constant $\Delta\varepsilon_v/\Delta\varepsilon_a$ when the soil element is at the
391 plastic state. As shown Fig. 5, the simulated results with the MMC model match well with the
392 test results not only the peak (like the MC model) but also for a wide range of strains
393 encountered in the pipeline–soil interaction analysis as presented in the following sections. It can
394 be also concluded that the parameters listed in Table 1 can simulate the stress–strain behaviour
395 of this sand. Adjustments to the values of A_ψ and k_ψ could improve matching between FE
396 simulations and test results; however, that is not the aim of the present study.

397 The effects of σ_c and D_r on stress–strain behaviour are also investigated. Figure 6(a) shows
398 the variation of q/p' with ε_a for 4 different confining pressures ($\sigma_c=20, 40, 80$ and 120 kPa) for
399 $D_r=80\%$. The maximum stress ratio $(q/p')_{\max}$ decreases with σ_c because dilation is suppressed by
400 confining pressure. The magnitude of ε_a at $(q/p')_{\max}$ increases with σ_c . Under lower confining
401 pressures, the post-peak degradation of q/p' occurs quickly. Figure 6(b) shows that the magnitude
402 and rate of development of ε_v depend on confining pressure. The soil specimens compress

403 initially (i.e. positive ε_v) and then dilate after reaching the maximum ε_v . For lower σ_c , dilation
404 starts at smaller value of ε_a . Moreover, the rate of dilation and maximum volumetric expansion
405 decrease with σ_c . The variations of q/p' and ε_v obtained from FE simulations using the proposed
406 MMC model (Figs. 6a and 6b) are very similar to typical triaxial test results on dense sand as
407 shown in Fig. 1(a) and 1(b).

408 Figure 7 shows the results of FE simulations for 4 relative densities ($D_r=70\%$, 80%, 90% and
409 100%) under the same σ_c (=40 kPa). Figure 7(a) shows that $(q/p')_{\max}$ increases and ε_a at $(q/p')_{\max}$
410 decreases with D_r . As expected, higher dilation is calculated for higher relative densities. Similar
411 effects of D_r on stress–strain behaviour were obtained in laboratory tests reported by previous
412 researchers (e.g. Lee 1965).

413 It is also noted here that simulations of drained triaxial tests with the MMC model give a
414 nonlinear critical state line in $e-\ln p'$ space.

415 In summary, the above simulations show that the proposed MMC model can successfully
416 simulate both pre- and post-peak behaviour of dense sand including the effects of confining
417 pressure and relative density. This model is primarily used for pipeline–soil interaction analyses
418 presented in the following sections, although some analyses with the MC model are performed
419 for comparison.

420 5. Model test simulation results

421 Figure 8 shows the variation of dimensionless lateral force N_h ($=F/\gamma HD$) with dimensionless
422 lateral displacement u/D for two burial depths ($H/D=1.5$ and 5.5). Here F is the lateral force on
423 the pipe per metre length, H is the depth of the centre of the pipe, γ is the unit weight of sand and
424 u is the lateral displacement. The peak value of N_h is defined as N_{hp} and the lateral displacement
425 required to mobilize N_{hp} is defined as u_p . Analyses are performed for the plane strain condition

426 ($A_\psi=5$ and $k_\psi=0.8$ in Eq. 1 and 2, respectively) using the user subroutine VUSDFLD. Using the
427 initial mean effective stress at the centre of the pipe the Young's modulus (E) is calculated from
428 Eq. (9), which implies that E increases with D_r and H . The results of two model tests of similar
429 conditions (Test-22 and 24) from Trautmann (1983) are also plotted in this figure. The force–
430 displacement curves obtained from the FE analysis with the MMC model match very well for a
431 wide range of lateral displacements. For $H/D=1.5$, the dimensionless force reaches the peak and
432 then remains almost constant. However, for $H/D=5.5$, the dimensionless force reaches the peak
433 and then decreases with further lateral displacement. The model tests conducted by Audibert and
434 Nyman (1977) using a 25 mm diameter pipe buried in dense Carver sand also show similar
435 response—no post-peak degradation of N_h for shallow depths ($H=1.5D$ and $3.5D$) but significant
436 post-peak degradation for deep burial conditions ($H=6.5D$ and $12.5D$).

437 The difference between the shape of the force–displacement curves could be explained further
438 using mobilized ϕ' and ψ along the shear bands and their formation. The role of ϕ' is easily
439 understood—the higher the ϕ' the higher the force, provided all other conditions remain same.
440 Figure 9(a) shows γ^p at $u/D=0.12$ (i.e. after the peak) for simulation with the MMC model. The
441 solid lines through the highly concentrated γ^p zone are drawn for further investigation of the
442 location of the shear bands for various conditions. To explain the role of ψ , two more analyses
443 are performed using the MC model for two values of ψ ($=16^\circ$ and 25°) but constant ϕ' ($=44^\circ$) for
444 $H/D=1.5$. The force–displacement curve for $\psi=16^\circ$ in Fig. 8 shows that N_h increases with
445 displacement and reaches the peak of $N_{hp}=8.4$. For $\psi=25^\circ$, $N_{hp}=8.8$ (not plotted in Fig. 8).
446 Similar to Fig. 9(a), the locations of the shear bands are obtained for $u/D=0.12$ and plotted in Fig.
447 9(b). The shear bands for $\psi=25^\circ$ are located outside the shear bands with $\psi=16^\circ$, which implies

448 that with increase in ψ the size of the failure wedge increases and that in turn produces higher
449 N_{hp} .

450 In the MMC model, ψ is not constant but varies with plastic shear strain (Fig. 3). Therefore, in
451 the simulations with the MMC, shear band formation due to post-peak reduction of shear
452 strength initiates when γ^p exceeds γ_p^p . With increase in lateral displacement of the pipe, strain
453 concentration further increases in the previously formed shear band; however, no significant
454 change in the location and orientation of the shear band is found in this case although ψ
455 gradually reduces to zero at large γ^p . To verify this, analyses have been performed with $\psi=0$ and
456 $\phi'=\phi'_c=35^\circ$ and a smaller failure wedge is found as shown in Fig. 9(b) and this gives $N_{hp}=6.45$. In
457 other words, the mobilized dilation angle during the initiation of the shear band influences the
458 shape of the failure wedge and thereby the reaction force.

459 Figure 9(a) also shows that the shear band reaches the ground surface at a displacement near
460 the peak. At this stage, the γ^p in the major portion of the shear band is sufficiently high to reduce
461 ϕ' almost to ϕ'_c and ψ to 0. Because ϕ' and ψ do not decrease with further increase in γ^p , the N_h
462 remains almost constant between $u/D=0.1$ and 0.4. However, if analysis is simplified by using
463 $\phi'=\phi'_c$ and $\psi=0$, a smaller failure wedge forms which gives lower reaction force.

464 The shear band formation for $H/D=5.5$ is different from that of $H/D=1.5$. The calculated γ^p
465 using the MMC model at $u/D=0.12$ is shown in Fig. 10(a). The mobilized ϕ' and ψ at this stage
466 are shown in Figs. 10(b) and 10(c), respectively. As shown in Fig. 3, the maximum values of ϕ'
467 and ψ are mobilized at γ_p^p , and therefore $\phi' < \phi'_p$ and $\psi < \psi_p$ in the pre-peak ($\gamma_p < \gamma_p^p$) and
468 also in the post-yield ($\gamma_p > \gamma_p^p$) conditions. In Figs. 10a–c, the post-peak condition ($\gamma_p > \gamma_p^p$) is

469 developed in the shear bands near the pipe (colored zone), while in the potential shear band
470 above this (gray zone) some plastic shear strains develop ($\gamma_p < \gamma_p^p$) but these remain in the pre-
471 peak shear zone. In the colored segments of the shear bands in Figs. 10(b) and 10(c), the
472 mobilized ϕ' and ψ are in the post-yield while in the gray segments they are in the pre-peak zone.
473 Unlike the simulation for $H/D=1.5$ (Fig. 9a), large segments of the plastic shear zone are in the
474 pre-peak condition (gray) which will gradually change to the post-yield condition with increasing
475 γ_p due to lateral displacement of the pipe. As the strength of the soil is reduced with γ_p , the post-
476 peak degradation of N_h is calculated for this H/D (Fig. 8). As the post-peak softening of stress–
477 strain behaviour is not considered, the MC model cannot simulate the degradation of N_h after the
478 peak as shown in Fig. 8.

479 In summary, the above analyses with the proposed MMC model show not only superior
480 simulation of the force–displacement response but also explain the possible mechanisms
481 involved through close examination of the roles of model parameters and burial depth. The peak
482 force could be matched using representative values of ϕ' and ψ in the MC model. However, if the
483 variation of mobilized ϕ' and ψ with plastic shear strain and mean effective stress is considered
484 the insight into the mechanisms of pipeline–soil interaction could be better explained.

485 However, it is noted here that FE element size influences the results when the analyses involve
486 post-peak softening behavior of the soil. Gylland (2012) presented a summary of regularization
487 techniques available in the literature to reduce mesh dependency. Robert (2010) used a simple
488 element size scaling rule for pipeline–soil interaction analysis. An improved regularization
489 technique, considering the orientation of the curved shear bands, likely involves considerable
490 additional complexity and will be left for a future study.

491 **6. Parametric study**

492 Guo and Stolle (2005) compiled a large number of test results from 11 experimental studies
493 and showed that various factors (e.g. H , D , D_r , ϕ') influence the dimensionless force N_h . A
494 parametric study is presented in this section in which only one parameter is varied while the
495 other parameters are kept constant as listed in Table 1, unless otherwise mentioned.

496 **6.1 Effect of H/D**

497 The H/D ratio could be varied by changing the value of H or D or both. To show the effects of
498 H/D , a total of 10 FE analyses are conducted with the MMC model for the following
499 configurations: (i) $D=102$ mm, $H/D=1.5, 5.5, 6, 10$; (ii) $D=150$ mm, $H/D=4, 6$; (iii) $D=300$ mm,
500 $H/D=2, 4, 6, 10$.

501 Figure 11 shows the force–displacement curves for a given H/D ($=6$) but for three different
502 diameters. At u_p , the mean effective stress p' around the pipe is higher for larger diameter pipe.
503 The higher p' has two effects: (i) lower mobilized ϕ' and ψ , and (ii) higher γ_p^p required to
504 mobilize ϕ'_p and ψ_p (cf. Fig. 3 and 6a). Because of these two reasons, the N_{hp} reduces and u_p/D
505 increases with diameter. Compiling the results of model tests in dense sand, Guo and Stolle
506 (2005) showed the trend of decreasing N_{hp} with increase in D . This implies that the present FE
507 analyses could successfully simulate this trend.

508 Figures 12 and 13 show the effects of H and D on force–displacement curves when one of
509 them is varied keeping the other one fixed. The increase of H or reduction of D , increases the
510 H/D ratio. In both cases (Figs. 12 and 13) N_{hp} and u_p/D increase with H/D , which is consistent
511 with model tests and FE results (Audibert and Nyman 1977; Trautmann 1983; Guo and Stolle
512 2005).

513 The peak dimensionless force N_{hp} is one of the main parameters used in current pipeline design
514 practice. The calculated values of N_{hp} with the MMC model are plotted with H/D ratio on Fig.
515 14. For comparison, the results of physical model tests and some FE analyses available in the
516 literature are also plotted on this figure. The N_{hp} increases with H/D . The present FE analyses
517 calculate lower rate of increase of N_{hp} at higher H/D ratio. This trend is similar to the model tests
518 of Dickin and Leung (1985). As discussed before, p' around the pipe increases with depth of
519 burial, and that reduces the mobilized ϕ' and ψ which in turn results in lower N_{hp} . If ϕ' and ψ are
520 independent of p' , higher values of N_{hp} could be obtained especially for larger H/D as shown in
521 Fig. 14 calculated by Yimsiri et al. (2004) with the MC model and Jung et al. (2013) who used
522 the MC model with post-peak softening. Guo and Stolle (2005) also investigated the effects of
523 pressure dependency and showed a significant increase in N_{hp} at low H/D when ϕ'_p increases
524 with p' and ψ remains constant. However, with the present MMC model, that increase of N_{hp} at
525 low H/D is not found because the maximum limit of $I_{R=4}$ is used (Bolton 1986; White et al.
526 2008) and in all the analyses with the MMC model ψ varies with plastic shear strain. A
527 comparison between the results for $D=102$ mm and 300 mm shows that a lower pipe diameter
528 gives consistently higher N_{hp} at a given H/D , which is consistent with the model test results
529 compiled by Guo and Stolle (2005) and Dickin and Leung (1985) as shown in Fig. 14. The
530 possible reasons behind this are explained in previous sections.

531 6.2 Effect of model parameters A_ψ and k_ψ

532 As discussed in Section 2, for the PS condition Bolton (1986) recommended $A_\psi=5.0$ for use in
533 Eq. (1). Analyzing test results on Toyoura sand, Chakraborty and Salgado (2010) recommended
534 $A_\psi=3.8$ for both TX and PS conditions. Figure 15 shows the force–displacement curves for

535 $A_\psi=3.8$ and 5.0 for different H/D but the same pipe diameter ($D=300$ mm). For a given I_R , ϕ'_c
536 and k_ψ , the peak friction angle ϕ'_p and dilation angle ψ_p increase with A_ψ as defined in Eqs. (1)
537 and (2), which increase the mobilized ϕ' and ψ (Eqs. 5–8). Because of this, N_{hp} increases with
538 A_ψ . Moreover, u_p/D also increases with A_ψ .

539 The soil failure due to lateral displacement of a buried pipe is generally categorized into two
540 simple modes, namely the “wedge” mode in shallow burial conditions and the “plow through”
541 mode in deep burial conditions (e.g. O’Rourke and Liu, 2012). For shallow burial in dense sand,
542 the drained lateral displacement of the pipe results in upward and lateral movement of a soil
543 wedge that is assumed to slide along either a straight (triangular wedge) or curved (log-spiral
544 wedge) line. On the other hand, for deep burial conditions, the lateral movement of the pipe
545 results in soil flow around the pipe with negligible deformation at the ground surface. Further
546 discussion on failure mechanisms is provided in the following sections.

547 A close examination of progressive development of shear bands shows that for $H/D=2$ and 4 the
548 wedge while for $H/D=10$ the plow through mode governs the response. For $H/D=6$, wedge type
549 of failure occurs when $A_\psi=3.8$ is used, while the failure is very similar to plow through mode for
550 $A_\psi=5.0$. In other words, in the transition zone (from shallow to deep) the failure mechanism is
551 influenced by this parameter, and therefore a significant difference between calculated N_h is
552 found for $H/D=6$.

553 Similar to A_ψ , different values of k_ψ were obtained from test results on different sands (Bolton
554 1986; Chakraborty and Salgado 2010; Xiao 2014). Figure 16 shows the force–displacement
555 curves for three different values of k_ψ . For a given $\phi'_p - \phi'_c$, the value of ψ_p increases with
556 decrease in k_ψ (Eq. 2), which increases mobilized ψ (Eqs. 6 and 8). As discussed before, the size

557 of the failure wedge increases with ψ , therefore the dimensionless force is higher for lower value
558 of ψ as shown in Fig. 16.

559 6.3 Effect of relative density of sand

560 As the focus of the present study is to model the response of pipelines in dense sand, the effects
561 of relative density are examined for D_r between 70% and 90% (Fig. 17). In the analyses, I_R in Eq.
562 (1) is calculated for given D_r . In addition, the unit weight of sand for a given D_r is calculated
563 using specific gravity of sand $G_s=2.74$ and maximum and minimum densities of 15.5 and 18.3
564 kN/m^3 (Trautmann 1983). Figure 17 shows that N_{hp} increases with D_r . However, there is no
565 significant difference between calculated N_h at large displacements for different D_r .

566

567 7. Failure Pattern

568 The soil failure mechanisms are explained using the formation of shear bands with lateral
569 displacements. Figures 18(a–c) show the plastic shear strain (field variable FV1 in Abaqus) for
570 three lateral displacements, shown by the points A, B and C in Fig. 13: (i) at N_{hp} ($u/D=0.12$) (ii)
571 at moderate displacement ($u/D=0.17$), and (iii) at large displacement ($u/D=0.4$). At $u/D=0.12$,
572 large plastic shear strains accumulate in narrow zones and two shear bands f_1 and f_2 are formed
573 (Fig. 18a). With increase in displacement (e.g. $u/D=0.17$) the shear bands f_1 and f_2 propagate
574 further upward and also an additional shear band f_3 is formed (Fig. 18b). At very large
575 displacements (e.g. $u/D=0.4$) all the shear bands reach to the ground surface (Fig. 18c). In other
576 words, the failure surfaces develop progressively and mobilized ϕ' and ψ in the shear band are
577 not constant until large displacements when the soil reaches the critical state. The plastic shear
578 strains in the soil elements outside the shear bands are negligible. Therefore, the soil elements

579 bounded by f_1 and f_3 displace upward and left as a wedge while another wedge formed by the
580 shear bands f_2 and f_3 sinks downward, which is shown by the instantaneous velocity vectors in
581 the right column of Fig. 18. The shear bands in Fig. 18(c) are very similar to model tests of
582 Turner (2004) in dense sand. Shear bands of almost similar pattern are also found in the FE
583 simulations with the MMC model for $H/D \leq 6$. Moreover, as shown in Figs. 18(a)–(c), significant
584 plastic strains develop in the shear band which could be successfully simulated using
585 Abaqus/Explicit without numerical issues due to significant mesh distortion.

586 The soil failure mechanisms at large displacements for $H/D=10$ (Fig. 19) are different
587 from Fig. 18. The plastic shear strain concentration mainly occurs near the pipe instead of
588 reaching the ground surface. The shear bands are not symmetric above and below the centre of
589 the pipe rather the shear bands propagate more above the pipe. Behind the pipe, the plastic shear
590 strains develop in a relatively large zone and sand moves into the gap created by pipe
591 displacements. The instantaneous velocity vectors show that the soil element flow mainly occurs
592 above the pipe. Jung et al. (2013) suggested that burial depths of $15\text{--}23D$ are required for the
593 symmetric flow of soil around the pipe. As the burial depth considered in this study is not
594 sufficient for flow around mechanism, N_{hp} increases monotonically with H/D even at $H/D=10$
595 (Fig. 14), which should approach a horizontal asymptote at large H/D (Jung et al. 2013).

596 597 **8. Conclusions**

598 The response of buried pipelines subjected to lateral ground movement is critical for safe and
599 reliable design of pipelines. In this study, the lateral pipeline–soil interaction is investigated
600 using comprehensive FE analyses. One of the key components that significantly influences the
601 success of FE analyses of pipeline–soil interaction is the constitutive behaviour used for
602 modeling the soil. In this study, a modified Mohr-Coulomb (MMC) model is proposed which has

603 limited complexity but sufficient to capture most of the important features of stress–strain
604 behaviour of dense sand such as the nonlinear pre- and post-peak variation of the angle of
605 internal friction and dilation angle with plastic shear strain, loading conditions, density and mean
606 effective stress. A method to implement the MMC in Abaqus using a user subroutine is
607 presented. The FE results with the MMC are compared with FE results obtained with the
608 conventional Mohr-Coulomb (MC) model and experimental results. The following conclusions
609 can be drawn from this study.

610 a) The failure surfaces develop progressively with lateral displacement of the pipe. The
611 mobilized ϕ' and ψ are not constant along the shear bands although constant values are used
612 in the conventional MC model.

613 b) The shear band formation and the mobilized values of ϕ' and ψ along the shear band
614 significantly influence the shape of the force–displacement curves. For the same sand, post-
615 peak degradation of N_h is observed at intermediate burial depth (e.g. $H/D=5.5$ in Fig. 8),
616 while N_h remains almost constant for shallow depths (e.g. $H/D=1.5$). The present MMC
617 model is shown capable of simulating this.

618 c) The mobilized dilation angle ψ significantly influences the shape of the failure wedge and
619 thus the reaction force on the pipeline.

620 d) The variation of calculated peak dimensionless force (N_{hp}) with H/D using the present
621 MMC model is consistent with previous experimental results and numerical analyses;
622 however, the pressure and plastic shear strain dependency of ϕ' and ψ in the MMC model
623 gives better simulation of lateral resistance (N_h) for a wide range of lateral displacements
624 including the post-peak reduction of N_h .

625 e) The depth of embedment for transition from shallow to deep failure mechanisms is
626 influenced by the soil parameters A_ψ . For a higher value of A_ψ , the plow through mechanism
627 develops at shallower depths resulting in higher lateral resistance.

628

629 **Acknowledgements**

630 The works presented in this paper have been supported by the Research and Development
631 Corporation of Newfoundland and Labrador and the Natural Sciences and Engineering Research
632 Council of Canada (NSERC).

633

634 **List of symbols**

635 The following abbreviations and symbols are used in this paper:

TX	Triaxial
PS	Plane strain
DS	Direct shear
MC	Mohr-Coulomb model with constant ϕ' and ψ
MMC	Modified Mohr-Coulomb model with mobilized ϕ' and ψ as Fig. 3
A_ψ	Slope of $(\phi'_p - \phi'_c)$ vs. I_R in Eq.(1)
m, C_1, C_2	Soil parameter (Eqs. 3 and 4)
D	Pipeline diameter
E	Young's modulus
H	Distance from ground surface to the centre of pipe
I_R	Relative density index
K	Material constant

K_0	Earth pressure coefficient at rest
N_h	Lateral dimensionless force
N_{hp}	Peak lateral dimensionless force
Q, R	Material constant (Bolton 1986)
k_ψ	Slope of $(\phi'_p - \phi'_c)$ vs. ψ_p in Eq. (2)
p'	Mean effective stress
q	Deviatoric stress
u	Lateral displacement of pipe
u_p	Lateral displacement at N_{hp}
μ	Friction coefficient between pipeline and soil
ν	Poisson's ratio
ε_a^p	Axial strain at the peak stress ratio
ε_1^p	Major principal plastic strain
ε_3^p	Minor principal plastic strain
σ_c	Confining pressure
ϕ'	Mobilized angle of internal friction
ϕ'_{in}	ϕ' at the start of plastic deformation
ϕ'_p	Peak friction angle
ϕ'_c	Critical state friction angle
ϕ'^{PS}_p	Peak friction angle in plane strain condition
ϕ'^{TX}_p	Peak friction angle in triaxial condition
ϕ'^{DS}	Angle of internal friction in direct shear test

ϕ_p^{DS}	Peak friction angle in direct shear condition
ϕ_μ	Pipe-soil interface friction angle
ψ	Mobilized dilation angle
ψ_p	Peak dilation angle
ψ_{in}	ψ at the start of plastic deformation (=0)
γ^p	Engineering plastic shear strain
γ_p^p	γ^p required to mobilize ϕ'_p
γ_c^p	Strain softening parameter

636

637 **References**

- 638 Ahmed, S.M.U. 1973. A study of the influence of confining pressure on the behaviour of sands.
639 M.Sc. Thesis, McGill University, Montreal, Canada.
- 640 Almahakeri, M., Fam, A., and Moore, I.D. 2012. The flexural behaviour of buried steel and
641 composite pipes pulled relative to dense sand: experimental and numerical investigation. 9th
642 Int. Conf. on Pipelines IPC2012, September 24–28, Calgary, AB, Canada. IPC 2012-90158.
643 pp. 9.
- 644 Almahakeri, M., Fam, A., and Moore, I.D. 2014. Experimental investigation of longitudinal
645 bending of buried steel pipes pulled through dense sand. Journal of Pipeline Systems
646 Engineering and Management, ASCE, **5**(2). doi: 10.1061/(ASCE)PS.1949-1204.0000141.
- 647 Almahakeri, M., Fam, A., and Moore, I.D. 2013. Longitudinal bending and failure of GFRP
648 pipes buried in dense sand under relative ground movement. Journal of Composites for
649 Construction, ASCE, **17**(5):702–710.

650 American Lifelines Alliance. 2005. Seismic design guidelines for water pipelines. American
651 Lifelines Alliance in partnership with the Federal Emergency Management Agency,
652 Washington, D.C. Available from www.americanlifelinesalliance.org [accessed 4 April
653 2015].

654 Audibert, J.M.E., and Nyman, K.J. 1978. Soil restraint against horizontal motion of pipes.
655 International Journal of Rock Mechanics and Mining Sciences and Geomechanics Abstracts,
656 **15**(2): A29–A29.

657 Bishop, A. W. 1961. Discussion on soil properties and their measurement. Proceedings of 5th
658 Int. Conf. on Soil mechanics and Foundation engineering, vol. III.

659 Bolton, M. D. 1986. The strength and dilatancy of sands. *Geotechnique*, **36**(1):65–78.

660 Burnett, A. J. 2015. Investigation of full scale horizontal pipe–soil interaction and large strain
661 behaviour of sand. MAsc. thesis, Queen’s University, Kingston, Ontario, Canada.

662 Chakraborty, T., and Salgado, R. 2010. Dilatancy and shear strength of sand at low confining
663 pressures. *Journal of Geotechnical and Geoenvironmental Engineering*, **136**(3):527–532.

664 Conforth, D.H. 1964. Some experiments on the influence of strain conditions on the strength of
665 sand. *Geotechnique*, **14**:143–167.

666 Dafalias, Y. F., and Herrmann, L. R. 1982. Bounding surface formulation of soil plasticity. *Soil*
667 *Mechanics–Transient and Cyclic Loads*. Pande, G. N. and Zienkiewicz, O. C., Eds., John
668 Wiley and Sons, New York, NY.

669 Dafalias, Y. F., and Manzari, M. 2004. Simple plasticity sand model accounting for fabric
670 change effects. *ASCE Journal of Engineering Mechanics*, **130**(6): 622–634.

671 Daiyan, N., Kenny, S., Phillips, R., and Popescu, R. 2011. Investigating pipeline–soil interaction
672 under axial–lateral relative movements in sand. *Canadian Geotechnical Journal*,
673 **48**(11):1683–1695.

674 Davis, E. H. 1968. Theories of plasticity and the failure of soil masses. In *Soil mechanics:*
675 *Selected topics* (ed. I. K. Lee), London: Butterworth. pp. 341–380.

676 Dickin, E.A., and Leung, C.F. 1983. Centrifugal model tests on vertical anchor plates. *Journal of*
677 *Geotechnical Engineering*, **109**(12):1503–1525.

678 DNV 2007 (Det Norske Veritas). DNV-OS-F101. Available from
679 <https://exchange.dnv.com/servicedocuments/dnv/> [accessed 4 April 2015].

680 Ellis, E.A., and Springman, S.M. 2001. Modelling of soil-structure interaction for a piled bridge
681 abutment in plane strain FEM analyses. *Computers and Geotechnics*, **28**(2):79–98.
682 doi:10.1016/S0266-352X(00)00025-2.

683 Gajo, A., and Muir Wood, D. 1999. A kinematic hardening constitutive model for sands: the
684 multiaxial formulation. *International Journal for Numerical and Analytical Methods in*
685 *Geomechanics*, **23**(9): 925–965.

686 Guo, P., and Stolle, D. 2005. Lateral pipe-soil interaction in sand with reference to scale effect.
687 *Journal of Geotechnical and Geoenvironmental Engineering*, **131**(3):338–349.

688 Gylland A. S. 2012. Material and slope failure in sensitive clays. PhD thesis, Norwegian
689 University of Science and Technology.

690 Hardin, B .O., and Black, W. L. 1966. Sand stiffness under various triaxial stress. *Journal of the*
691 *Soil Mechanics and Foundations Division, ASCE*, **92**(SM2):27–42.

692 Hashiguchi, K., and Ueno, M. 1977. Elastoplastic constitutive laws of granular materials,
693 Constitutive Equations of Soils. Proc. 9th Int. Conf. Soil Mech. Found. Eng., Spec. Session S,
694 eds. Murayama, S. and Schofield, A. N., JSSMFE, Tokyo. pp. 73–82.

695 Honegger, D., and Nyman, D.J. 2004. Guidelines for the seismic design and assessment of
696 natural gas and liquid hydrocarbon pipelines. Pipeline Research Council International,
697 Catalog No. L51927, October.

698 Houlsby, G.T. 1991. How the dilatancy of soils affects their behaviour. Invited Theme Lecture,
699 Proceedings of the Tenth European Conference on Soil Mechanics and Foundation
700 Engineering, Florence, May 27-30, Vol. 4, ISBN 90-5410-005-2. pp. 1189–1202.

701 Hsu, S.T., and Liao, H.J. 1998. Uplift behaviour of cylindrical anchors in sand. Canadian
702 Geotechnical Journal, **35**(1):70–80.

703 Janbu, N. 1963. Soil compressibility as determined by oedometer and triaxial tests. Proceedings,
704 European Conference on Soil Mechanics and Foundations Engineering, Wiesbaden,
705 Germany, Vol. 1. pp.19–25.

706 Jardine, R. J. 1992. Nonlinear stiffness parameters from undrained pressuremeter Tests.
707 Canadian Geotechnical Journal, **29**(3):436–447. doi: 10.1139/t92-048.

708 Jefferies, M., and Been, K. 2000. Soil liquefaction: a critical state approach. Taylor & Francis,
709 New York.

710 Jung, J., O'Rourke, T., and Olson, N. 2013. Lateral soil-pipe interaction in dry and partially
711 saturated sand. Journal of Geotechnical and Geoenvironmental Engineering, **139**(12):
712 2028–2036.

713 Jung, J., O'Rourke, T., and Olson, N. 2013. Uplift soil–pipe interaction in granular soil. Canadian
714 Geotechnical Journal, **50**(7):744–753. doi: 10.1139/cgj-2012-0357.

715 Kolymbas, D, and Wu, W. 1990. Recent results of triaxial tests with granular materials. Powder
716 Technology, **60**(2):99–119.

717 Kouretzis, G.P., Sheng, D., and Sloan, S.W. 2013. Sand-pipeline-trench lateral interaction effects
718 for shallow buried pipelines. Computers and Geotechnics, **54**:53-59.

719 Kulhawy, F.H., and Mayne, P.W. 1990. Manual on estimating soil properties for foundation
720 design. Report EPRI-EL 6800, Electric Power Research Institute, Palo Alto. pp. 306.

721 Lancelot, L, Shahrour, I, and Mahmoud, MA. 2006. Failure and dilatancy properties of sand at
722 relatively low stresses. J. Eng. Mech, ASCE, **132**(12):1396 –1399.

723 Lee, K. L., and Seed, H. B. 1965. Drained strength characteristics of sands. Journal of the Soil
724 Mechanics and Foundations Division, ASCE, **93**(6):117–141.

725 Lings, M. L., and Dietz, M. S. 2004. An improved direct shear apparatus for sand. Geotechnique,
726 **54**(4):245–256.

727 Mitchell, J.K., and Soga, K., 2005. Fundamentals of soil behavior. 3rd Edition. John Wiley &
728 Sons, Hoboken.

729 Moore, I.D. and Booker, J.R., 1987. Ground failure around buried tubes. International Journal
730 of Rock Mechanics and Rock Engineering, **20**(4):243–260.

731 Mroz, Z. 1967. On the description of anisotropic work hardening. J. Mech. Phys. Solids.
732 **15**:163–175.

733 O'Rourke, and M.J., Liu, X. 2012. Seismic design of buried and offshore pipelines. MCEER
734 Monograph, MCEER-12-MN04.

735 Pike, K., Kenny, S., and Hawlader, B. 2013. Advanced analysis of pipe/soil interaction
736 accounting for strain localization. Proceeding, GéoMontréal 2013, the 66th Canadian

737 Geotechnical Conference and the 11th Joint CGS/IAH-CNC Groundwater Conference,
738 Montreal, Canada.

739 Pradhan, T.B.S., Tatsuoka, F., and Horii, N. 1988. Strength and deformation characteristics of
740 sand in torsional simple shear. *Soils and Foundations*, **28**(3):131–148.

741 Prevost, J.H. 1985. A simple plasticity theory for frictional cohesionless soils. *Soil Dynamics*
742 *and Earthquake Engineering*, **4**(1): 9–17.

743 Qiu G, Henke S, and Grabe J. 2009. Applications of coupled Eulerian–Lagrangian method to
744 geotechnical problems with large deformations. Proceeding of SIMULIA customer
745 conference 2009, London, UK. pp. 420–435.

746 Robert, D. J. 2010. Soil-pipeline interaction in unsaturated soils. PhD thesis, University of
747 Cambridge, United Kingdom.

748 Rowe, P. W. 1969. The relation between the shear strength of sands in triaxial compression,
749 plane strain and direct shear. *Geotechnique*, **19**(1):75–86.

750 Scarpelli, G., Sakellariadi, E., and Furlani, G. 1999. Longitudinal pipeline–soil interaction:
751 results from field full scale and laboratory testing. Twelfth European Conference on Soil
752 Mechanics and Geotechnical Engineering. pp. 511.

753 Schanz, T., and Vermeer, P. A. 1996. Angles of friction and dilatancy of sand. *Geotechnique*,
754 **46**(1):145–151.

755 Simoni, A., and Houlsby, G. T. 2006. The direct shear strength and dilatancy of sand-gravel
756 mixtures. *Geotechnical & Geological Engineering*, **24**(3):523–549.

757 Taleb, B. and Moore, I.D., 1999. Metal culvert response to earth loading – Performance of
758 two–dimensional analysis. Transportation Research Record No. 1656, Underground and
759 Other Structural Design Issues. National Research Council, Washington. pp. 25–36.

760 Tatsuoka, F., Sakamoto, M., Kawamura, T., and Fukushima, S. 1986. Strength and deformation
761 characteristics of sand in plane strain compression at extremely low pressures. *Soils and*
762 *Foundations*, **26**(1):65–84.

763 Tatsuoka, F., Siddiquee, M. S. A., Park, C-S, Sakamoto, M. and Abe, F. 1993. Modeling stress–
764 strain relations of sand. *Soils and Foundations*, **33**(2):60–81.

765 Taylor, D. W. 1948. *Fundamentals of soil mechanics*. New York: Wiley.

766 Trautmann, C. 1983. Behavior of pipe in dry sand under lateral and uplift loading. PhD thesis,
767 Cornell University, Ithaca, NY.

768 Turner, J. P., and Kulhawy, F. H. 1987. Experimental analysis of drilled shaft foundations
769 subjected to repeated axial loads under drained conditions. Rep. to Electric Power Research
770 Institute, Cornell University, Ithaca, NY.

771 Turner, J.E. 2004. Lateral force–displacement behavior of pipes in partially saturated sand. M.S.
772 Thesis, Cornell University, Ithaca, NY.

773 Vermeer, P. A. and de Borst, R. 1984. Non-associated plasticity for soils, concrete and rock.
774 *HERON*, **29**(3):1–64.

775 White, D. J., Cheuk, C. Y., and Bolton, M. D. 2008. The uplift resistance of pipes and plate
776 anchors buried in sand. *Geotechnique*, **58**(10), 771–777.

777 Wijewickreme, D., Karimian, H., and Honegger, D. 2009. Response of buried steel pipelines
778 subjected to relative axial soil movement. *Canadian Geotechnical Journal*, **46**(7):735–735.

779 Wood, D. M. 2007. The magic of sands — The 20th Bjerrum Lecture presented in Oslo, 25
780 November 2005. *Canadian Geotechnical Journal*, **44**(11):1329–1350. doi: 10.1139/T07-060.

781 Xie, X. 2008. Numerical analysis and evaluation of buried pipeline response to earthquake-
782 induced ground fault rupture. PhD thesis, Rensselaer Polytechnic Institute, New York.

- 783 Xiao, Y., Liu, H., Chen, Y., and Chu, J. 2014. Strength and dilatancy of silty sand. ASCE Journal
784 of Geotechnical and Geoenvironmental Engineering, **140**(7).
- 785 Yimsiri, S., Soga, K., Yoshizaki, K., Dasari, G., and O'Rourke, T. 2004. Lateral and upward soil-
786 pipeline interactions in sand for deep embedment conditions. Journal of Geotechnical and
787 Geoenvironmental Engineering, **130**(8):830–842.
- 788 Yimsiri, S. and Soga, K. 2006. DEM analysis of soil–pipeline interaction in sand under lateral
789 and upward movements at deep embedment. Journal of Southeast Asian Geotechnical
790 Society, **37**:83–94.
- 791 Yoshimine, M. 2005. Archives–soil mechanics laboratory. Tokyo Metropolitan University,
792 Retrieved from <http://geot.civil.ues.tmu.ac.jp/archives/> [accessed 4 April 2015]

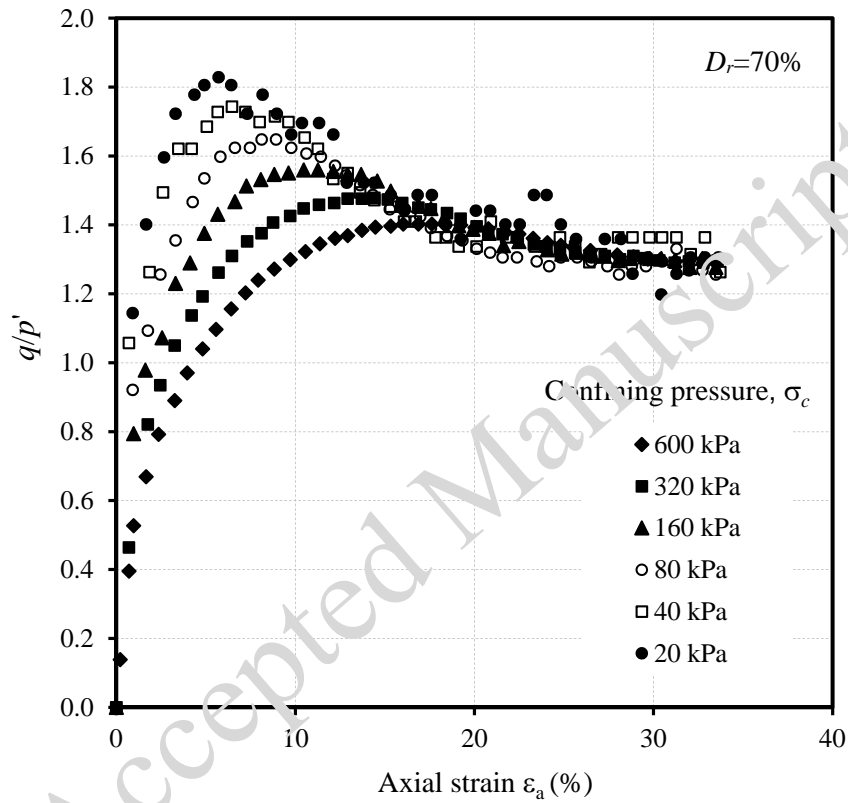


Fig. 1. Consolidated isotropically drained triaxial test results on dense sand (after Hsu and Liao 1998): (a) stress–strain behaviour

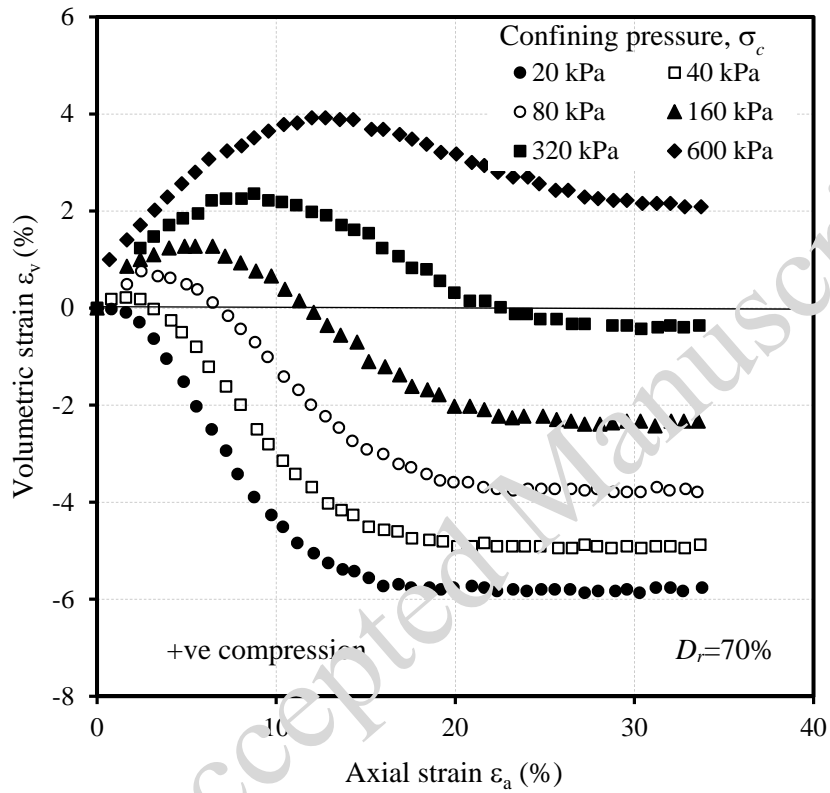


Fig. 1. Consolidated isotropically drained triaxial test results on dense sand (after Hsu and Liao 1998): (b) volume change behaviour

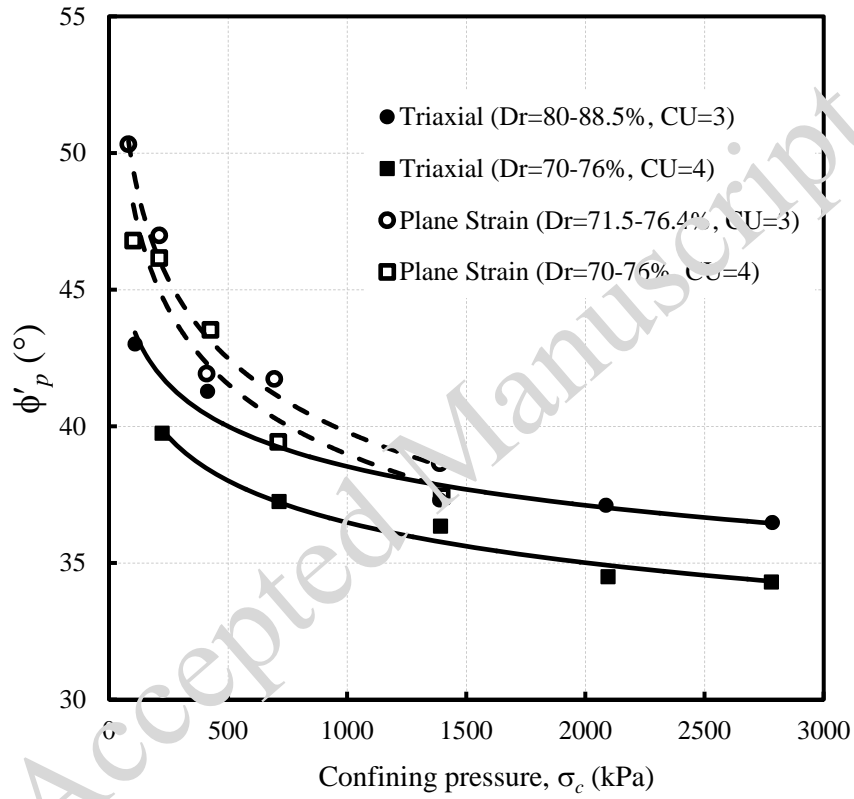


Fig. 2. Peak friction angle of crushed silica sand from triaxial and simple shear tests (after Ahmed 1973)

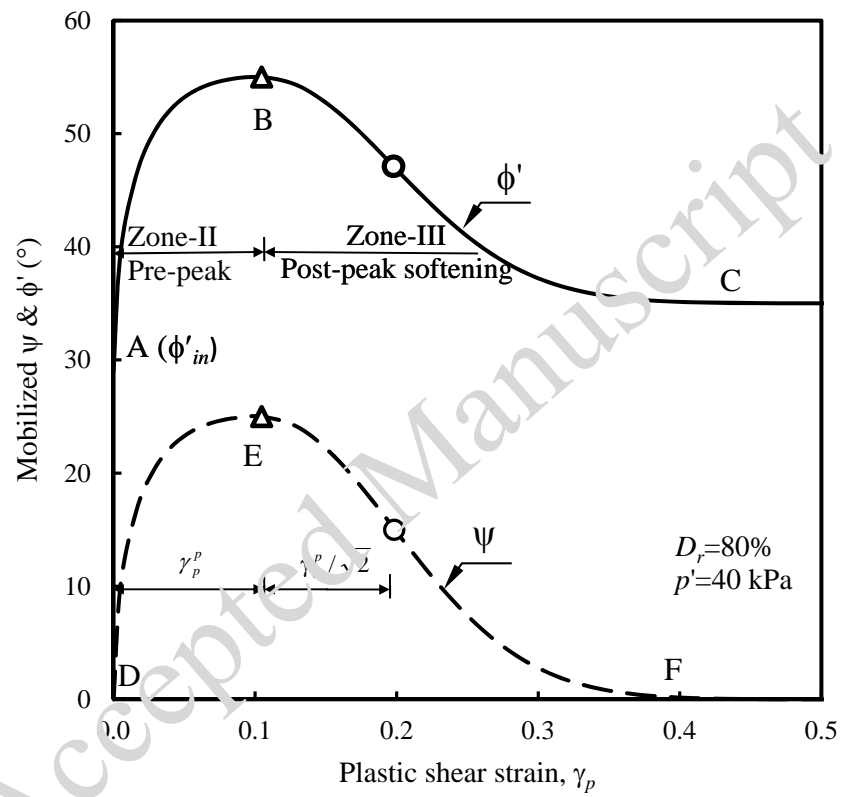


Fig. 3. Modeling of stress–strain behavior of dense sand using modified Mohr-Coulomb (MMC) model (plane strain condition)

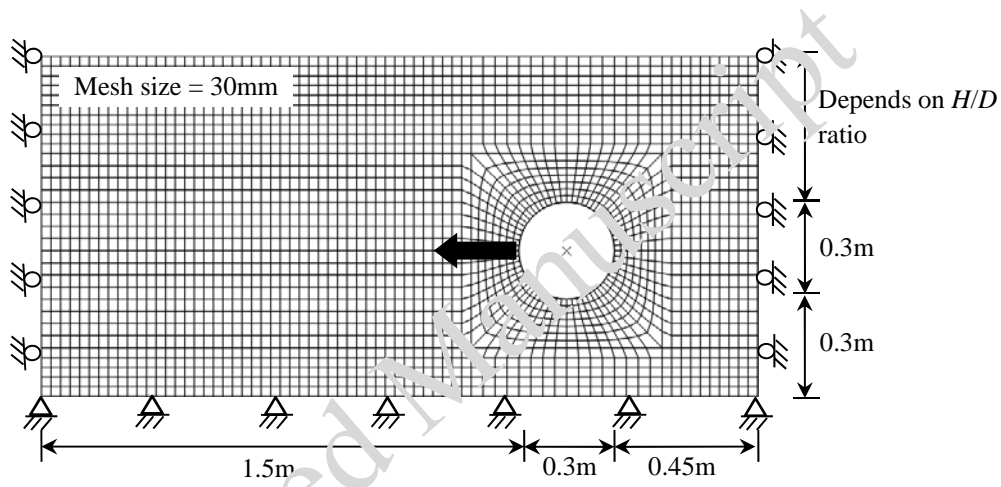


Fig. 4. Typical finite element mesh for $H/D=2$ and $D=300$ mm

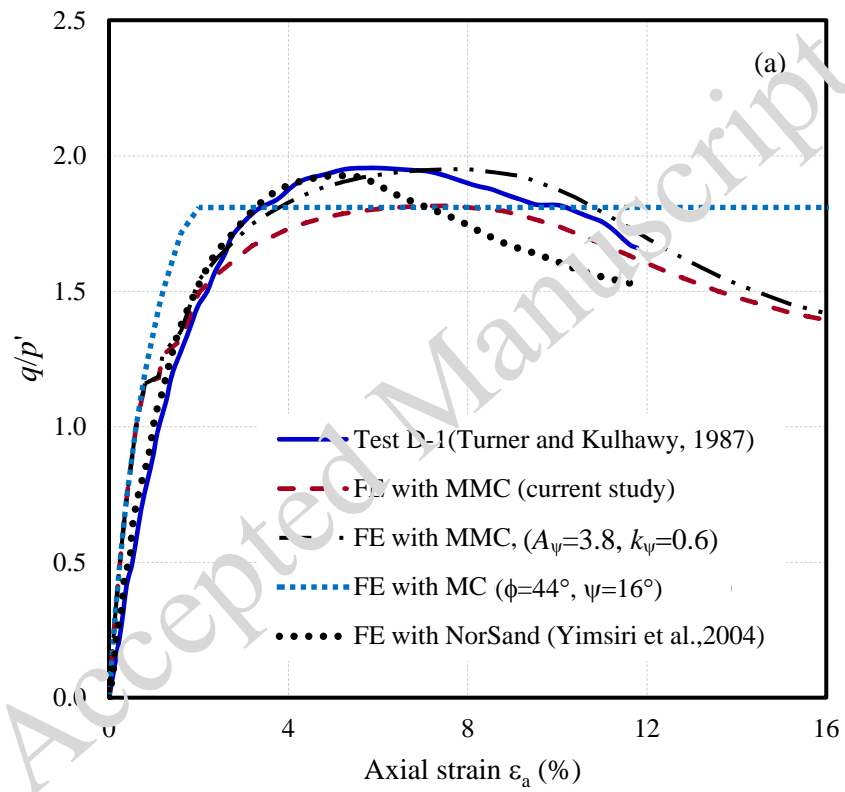


Fig. 5. Comparison of FE and triaxial compression tests results ($\sigma_c=39$ kPa, $D_r=80\%$): (a) stress-strain behaviour

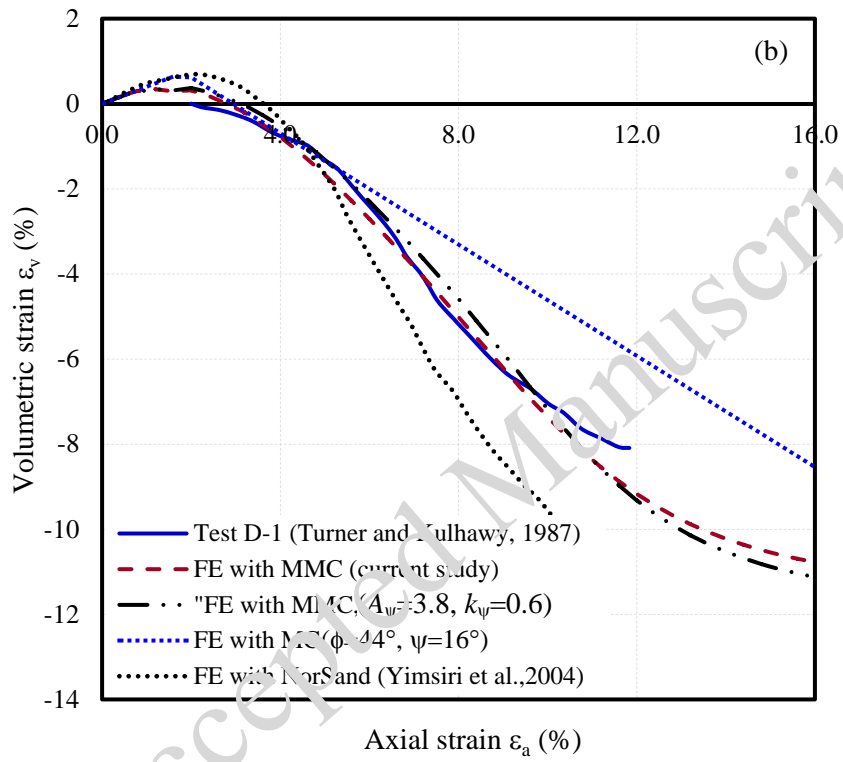


Fig. 5. Comparison of FE and triaxial compression tests results ($\sigma_c=39$ kPa, $D_r=80\%$): (b) volume change behaviour

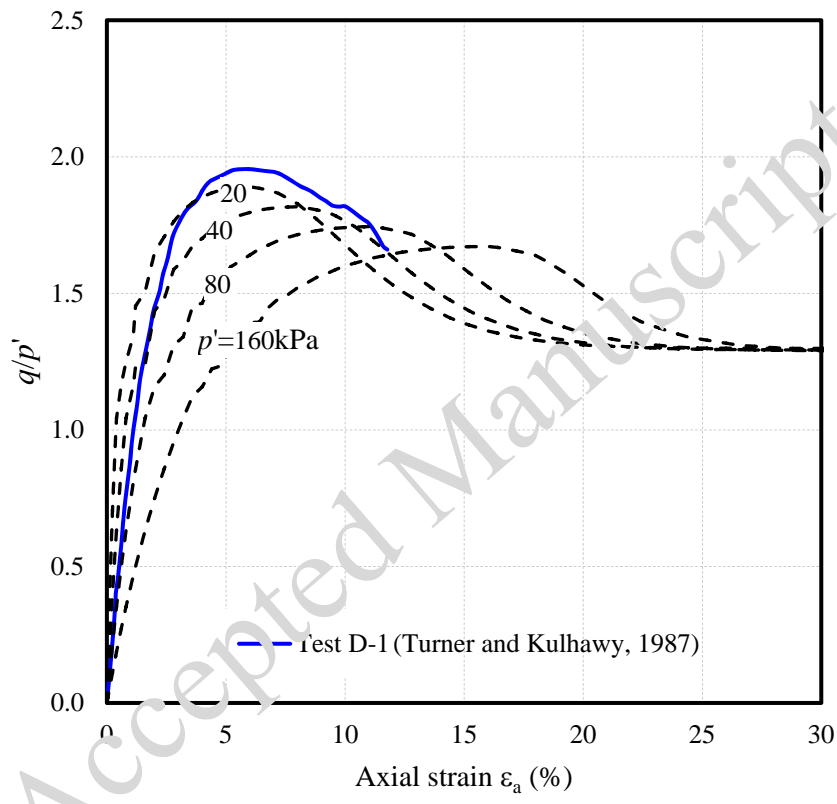


Fig. 6. Effect of confining pressure on triaxial tests ($D_r=80\%$): (a) stress–strain behaviour

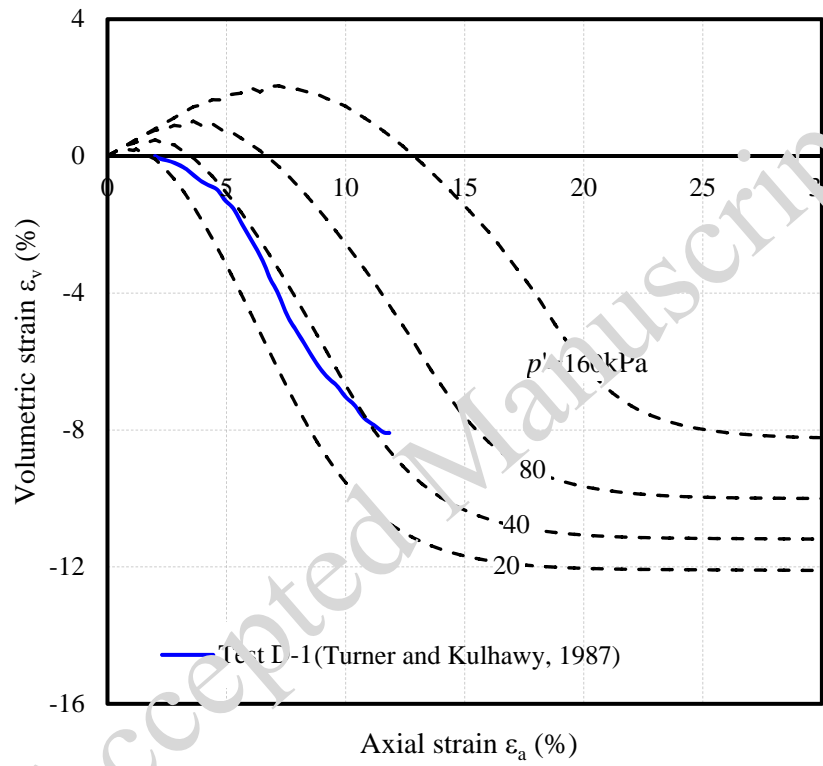


Fig. 6. Effect of confining pressure on triaxial tests ($D_r=80\%$): (b) volume change behaviour

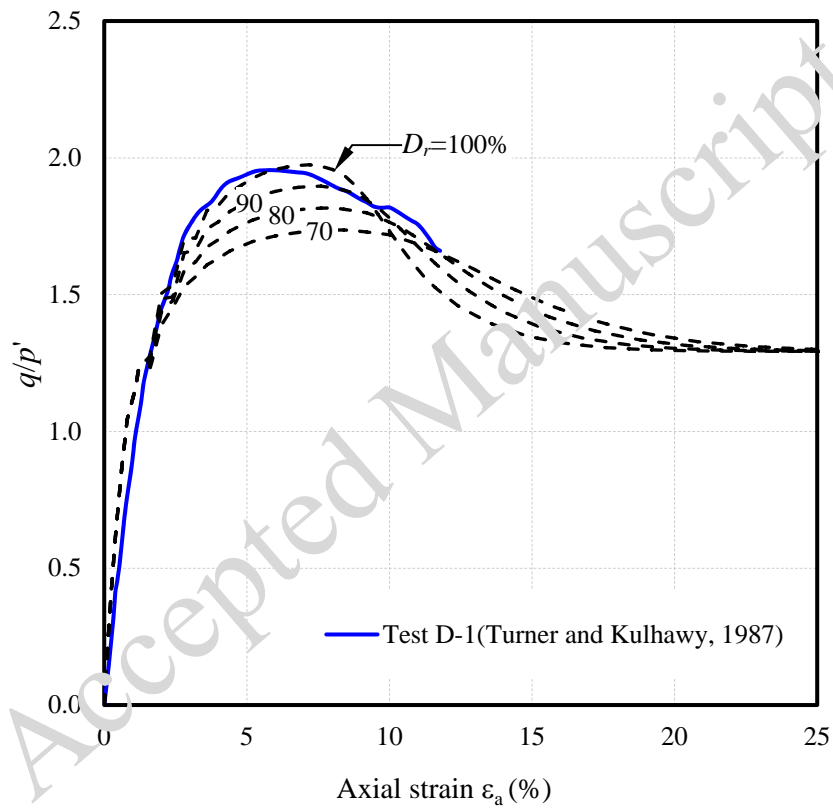


Fig. 7. Effect of relative density: (a) stress–strain behaviour

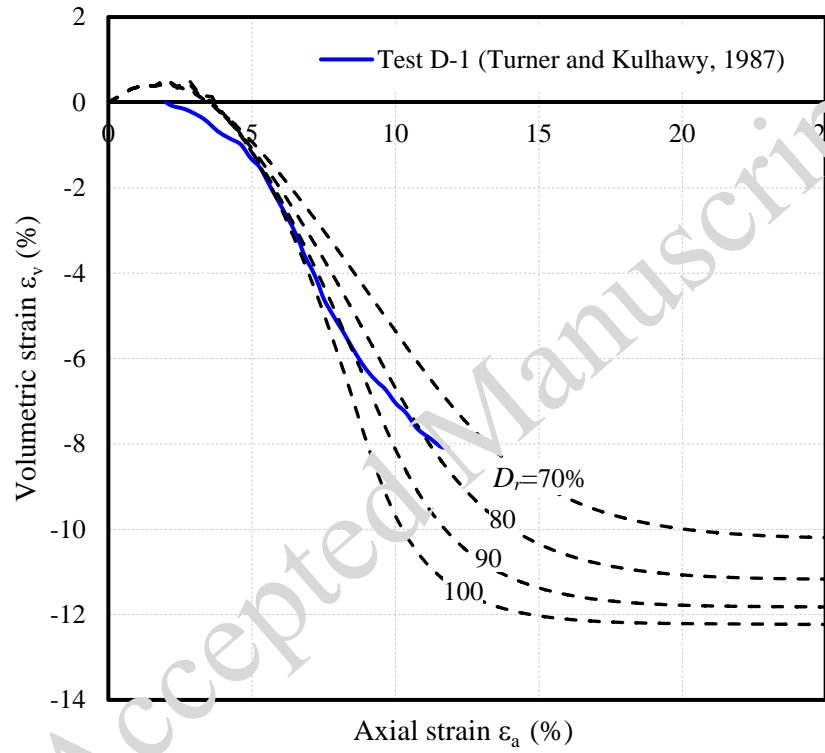


Fig. 7. Effect of relative density: (b) volume change behaviour

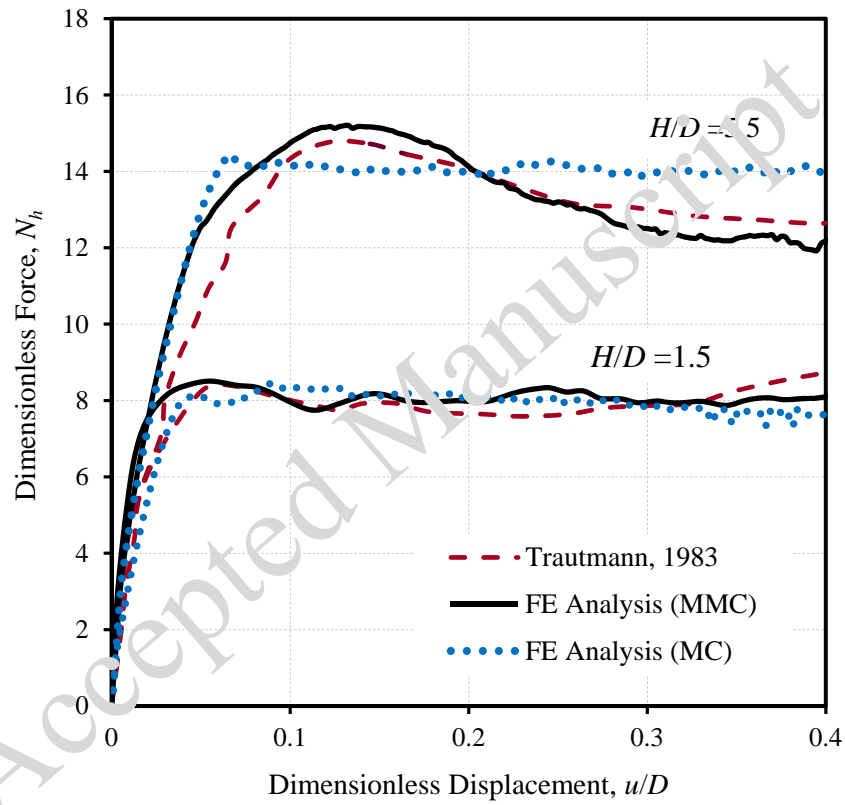


Fig. 8. Comparison of FE results with the large scale test results (Trautmann, 1983)

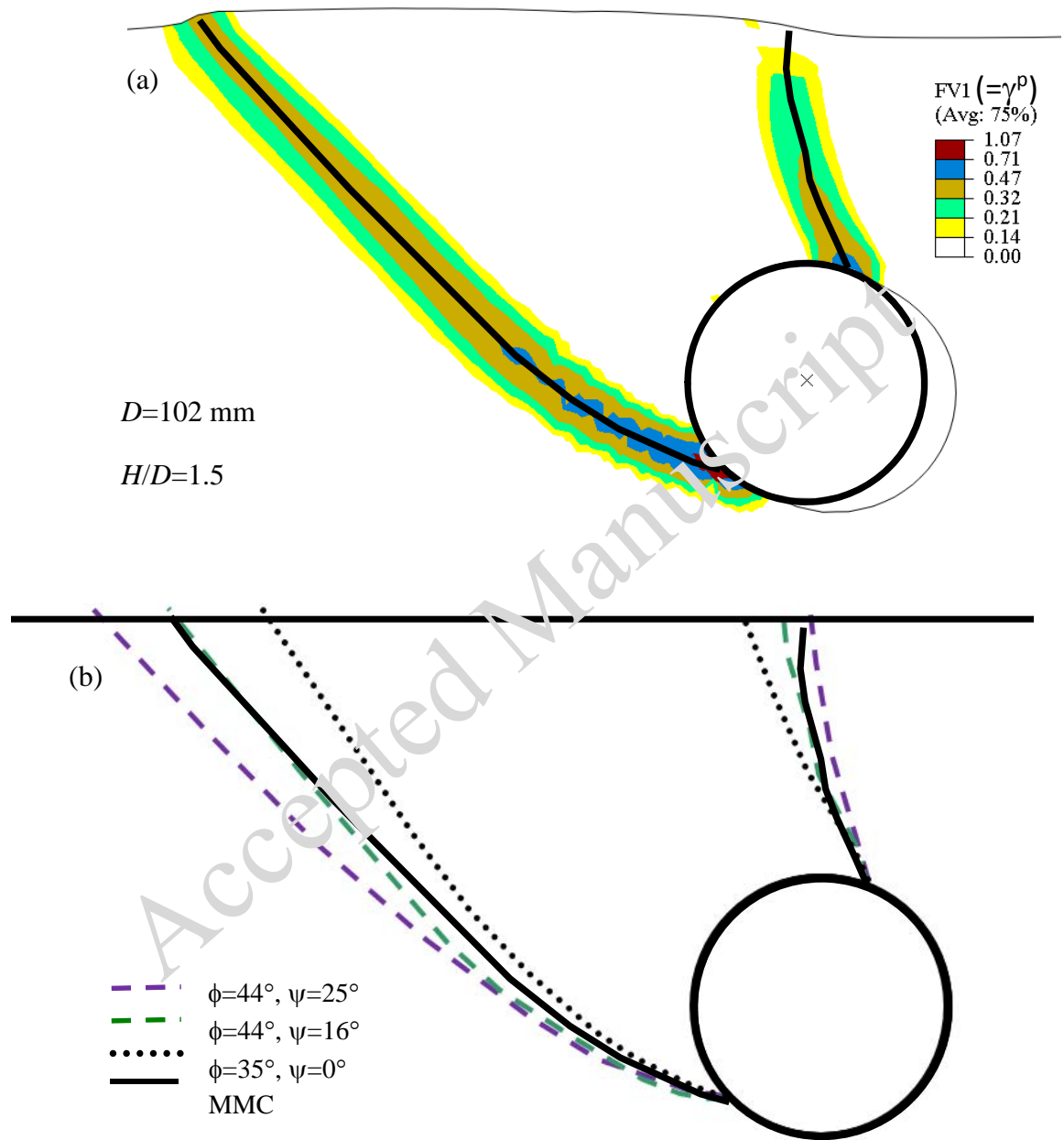


Fig. 9. Location of shear band at $u/D=0.12$: (a) using MMC (b) using MC and MMC model

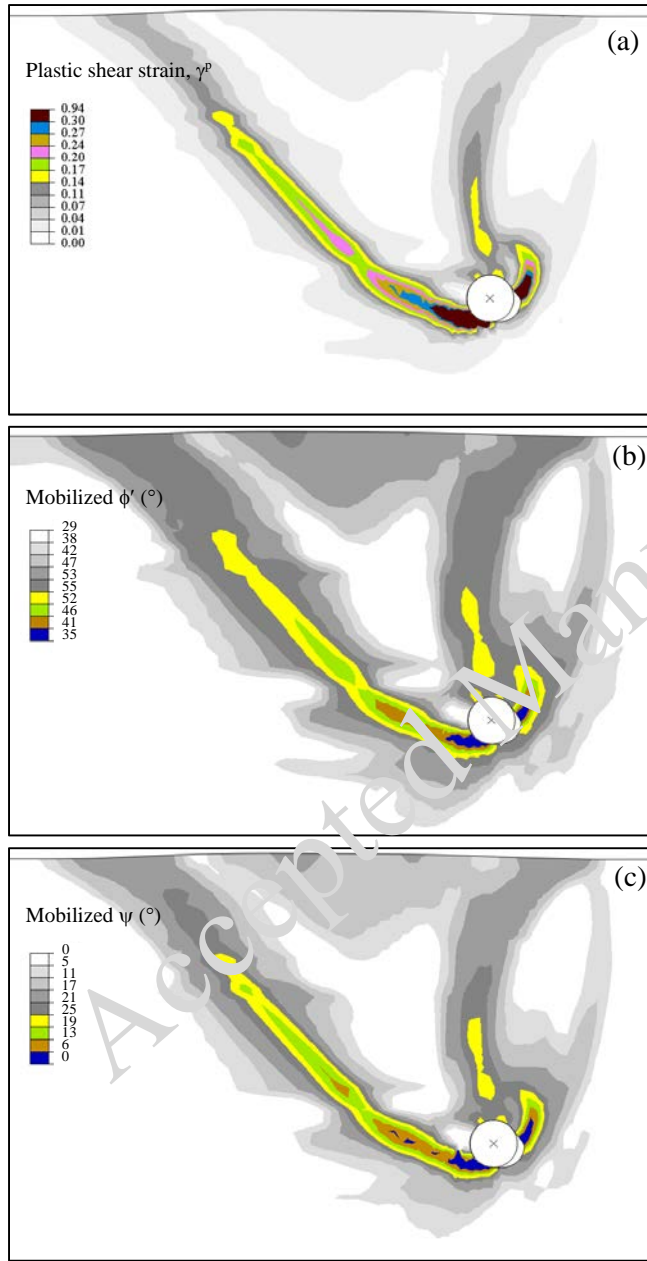


Fig. 10. Shear band formation and strength mobilization for $H/D=5.5$ and $D=102$ mm at $u/D=0.12$ with MMC model: (a) plastic shear strain γ^p , (b) mobilized ϕ' , (c) mobilized ψ

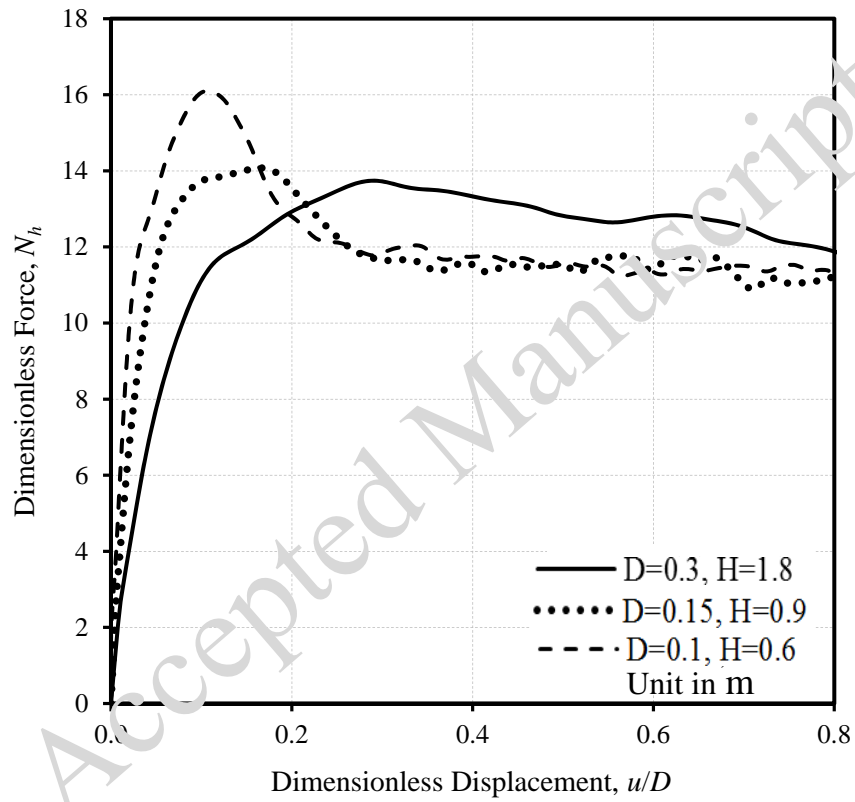


Fig. 11. Effects of diameter on force-displacement curve for $H/D=6$

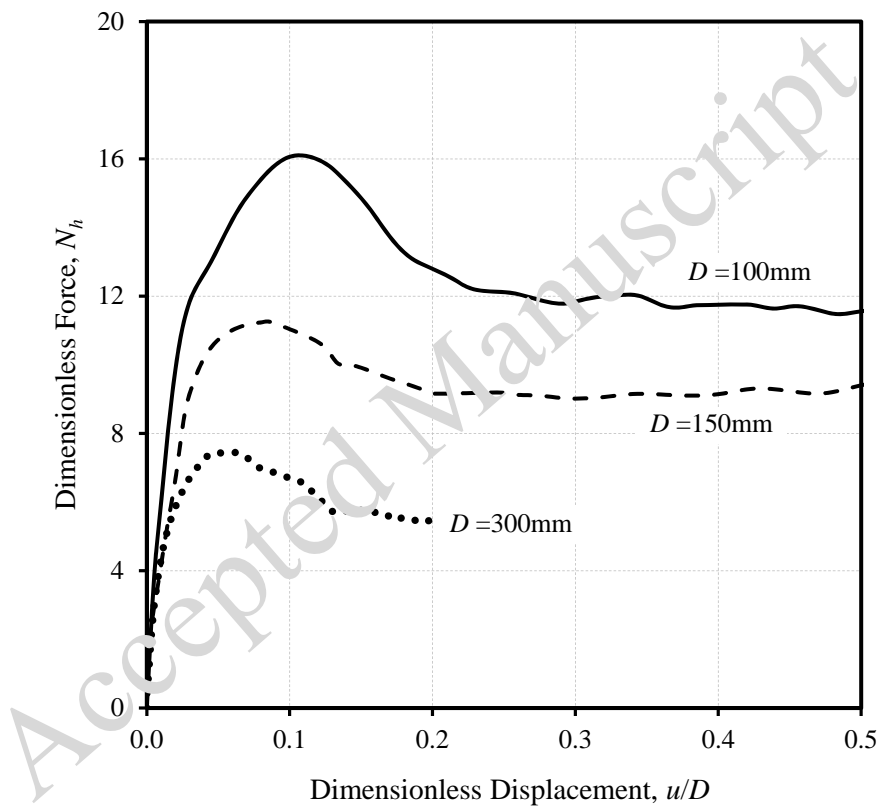


Fig. 12. Effect of pipe diameter on N_h for $H=600$ mm

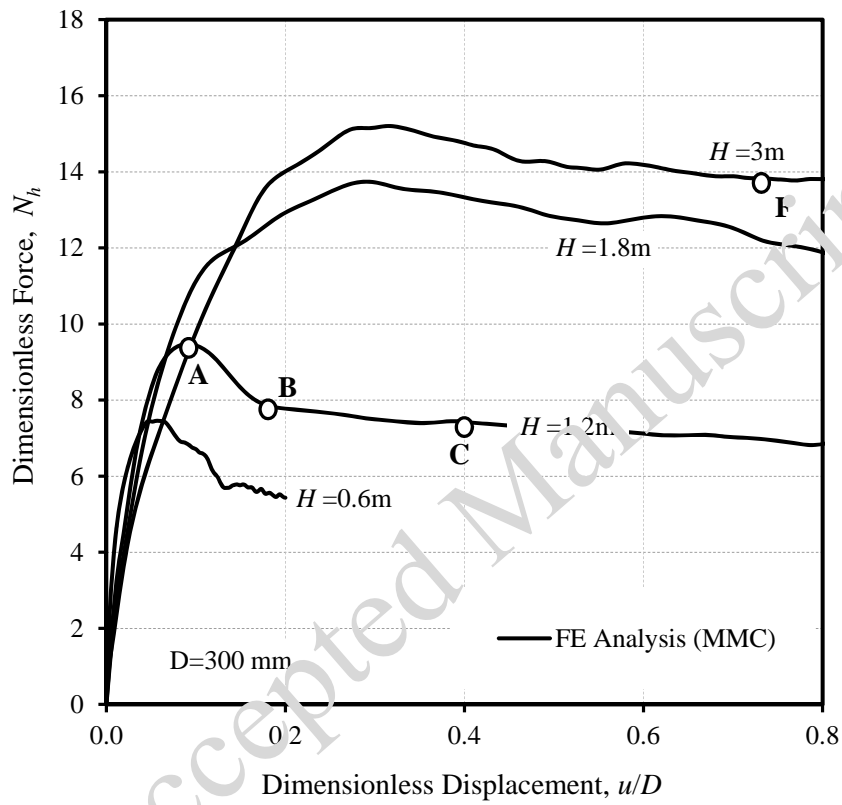


Fig.13. Effects of burial depth on N_h for $D=300$ mm

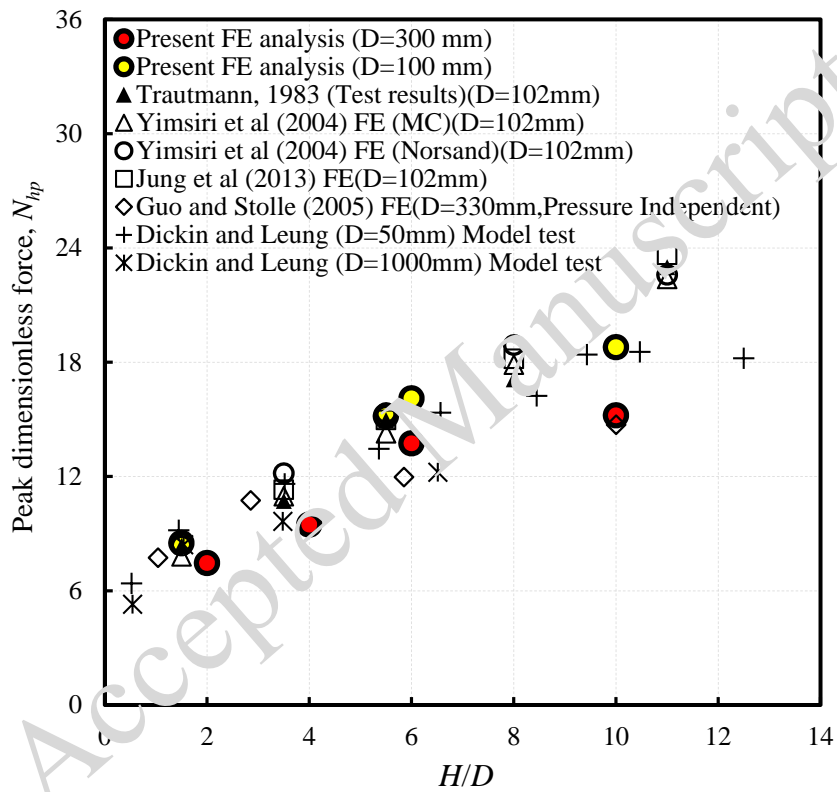


Fig. 14. Comparison of peak resistance N_{hp} with previous studies

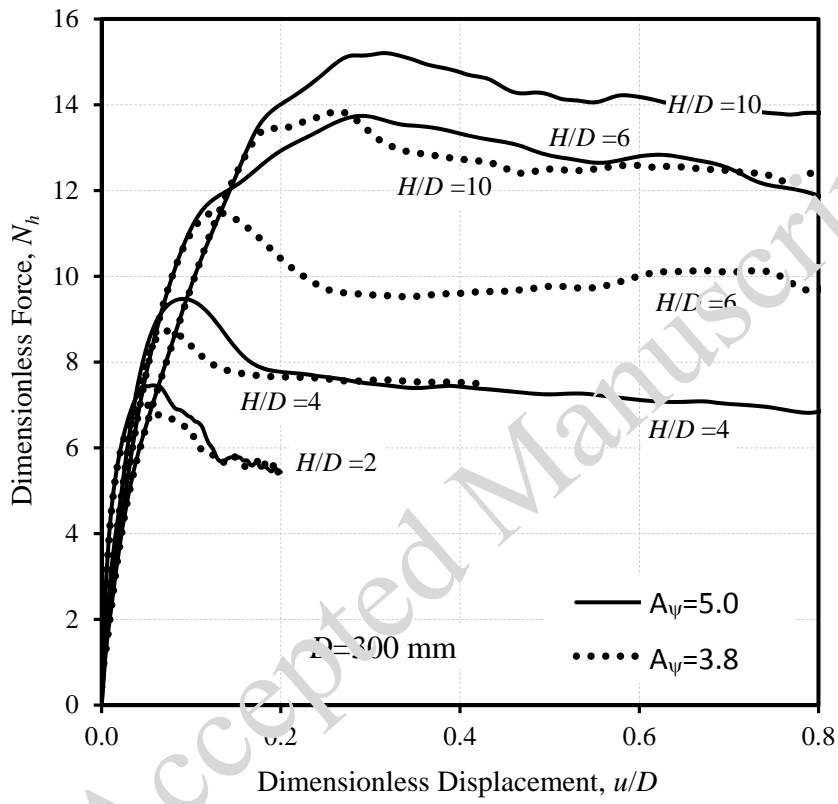


Fig. 15. Effect of A_ψ on dimensionless force N_h for $D=300$ mm

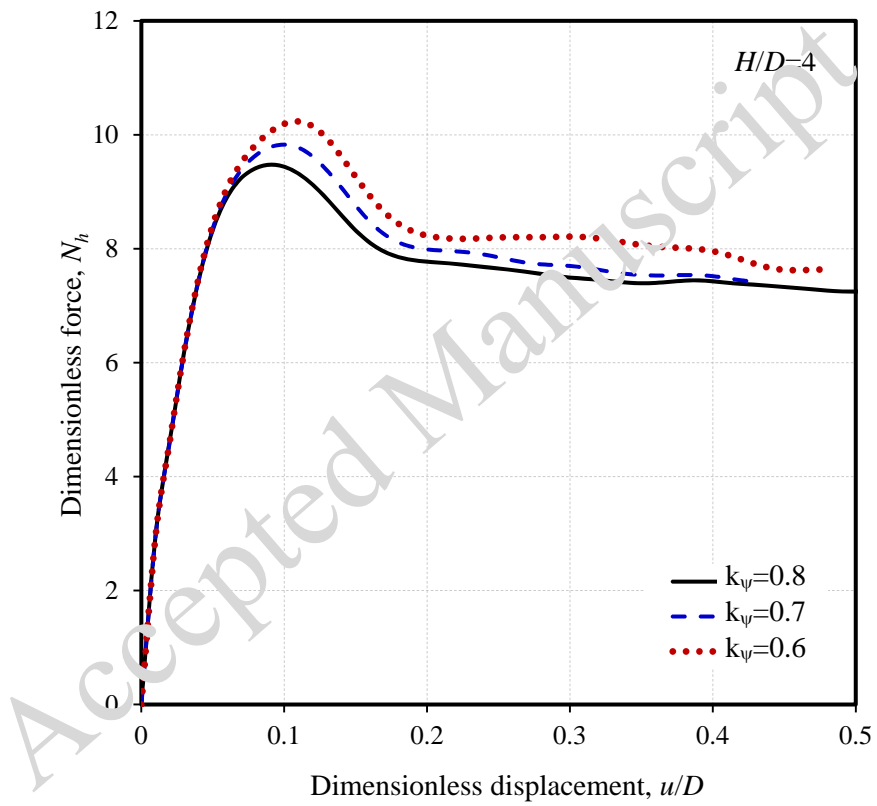


Fig. 16. Effect of k_ψ on dimensionless force N_h for $H/D=4$ and $D=300$ mm

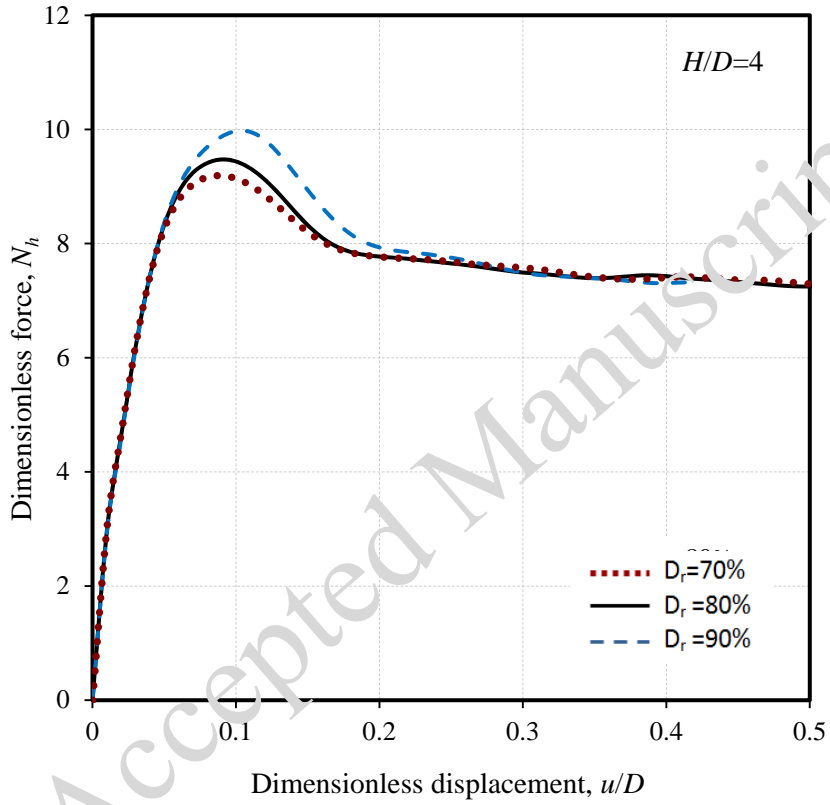


Fig. 17. Effect of relative density on dimensionless force N_h for $H/D=4$ and $D=300$ mm

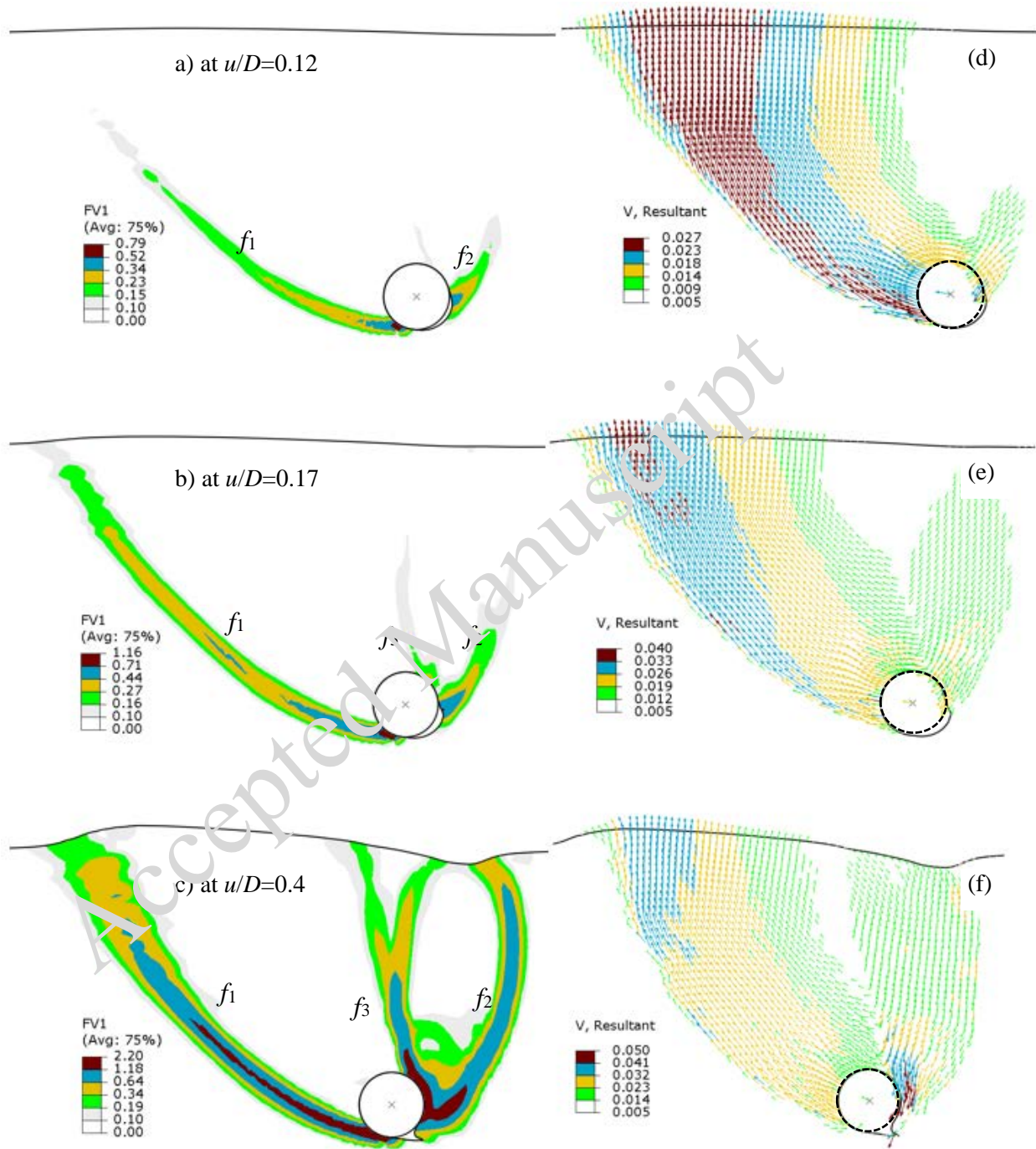


Fig. 18. Strain localization and instantaneous velocity vectors for $H/D=4$ and $D=300$ mm

(g) Model test (after Turner 2004)

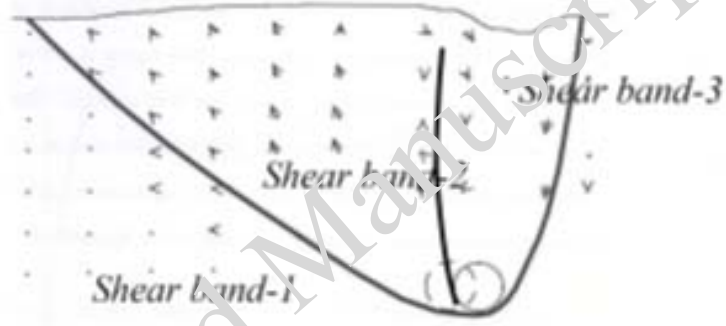
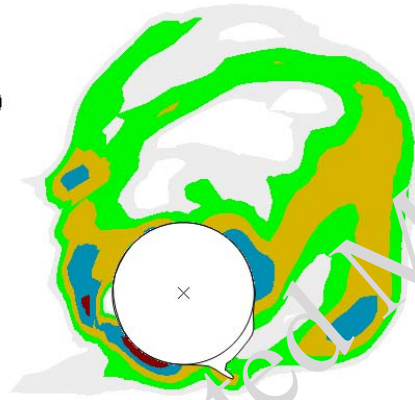


Fig. 18 (cont)

FV1
(Avg: 75%)

2.48
1.87
1.41
1.06
0.80
0.60
0.00



V, Resultant

0.020
0.017
0.015
0.012
0.010
0.007
0.005

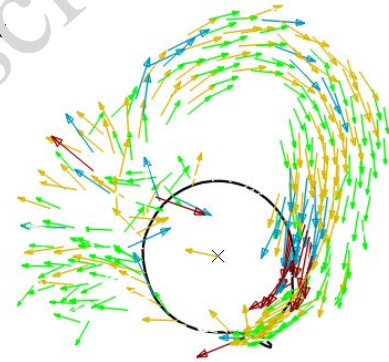


Fig. 19. Plastic shear strain and velocity vectors for $H/D=10$ and $D=300$ mm at $u/D=0.72$

Table 1: Geometry and soil parameters used in the FE analyses

Parameter	Triaxial test	Model test (Parametric Study)
External diameter of pipe, D (mm)	-	102 (100, 150, 300)
K	150	150
n	0.5	0.5
p_a (kN/m ²)	100	100
v_{soil}	0.2	0.2
A_{ψ}	3	5 (3, 3.8, 5)
k_{ψ}	0.5	0.8 (0.6, 0.7, 0.8)
ϕ'_{in}	29°	29°
C_1	0.22	0.22
C_2	0.11	0.11
m	0.25	0.25
Critical state friction angle, ϕ'_c	31°	35°
Relative density, D_r (%)	70, 80, 90, 100	80 (70, 80, 90)
Unit weight, γ (kN/m ³)	-	17.7 (17.31, 17.7, 18.12)
Interface friction coefficient, μ	-	0.32
Depth of pipe, H/D	-	1.5 & 5.5 (2, 4, 6, 10)

Note: Numbers in parenthesis in right column show the values used in the parametric study